**Revision 1 of Manuscript Number: 8715**

Word count: 8311 (excluding references); 11096 (total)

# Origin of clinopyroxene-ilmenite symplectites in mafic granulites from eastern parts of the Chotanagpur granite gneissic complex, East Indian shield.

SOMPDIPTA CHATTERJEE[1]*, SHREYA KARMAKAR[2], SUBHAM MUKHERJEE[3], SNAJOY SANYAL[1], PULAK SENGUPTA[1]

[1]Department of Geological Sciences, Jadavpur University, Kolkata 700032

[2]Department of Earth and Environmental Studies, National Institute of Technology, Durgapur 713209

[3]Department of Geology, University of Delhi, New Delhi 110007

*Corresponding author:

Name: Sompdipta Chatterjee

Email ID: somdipta.chatterjee@gmail.com

## ABSTRACT

In this manuscript, we report a rare occurrence of rod-like intergrowths of clinopyroxene-ilmenite that variably replace titanite in a suite of high pressure mafic granulites from the Chotanagpur Granite Gneissic Complex, Eastern Indian Shield. Garnet proximal to the clinopyroxene-ilmenite intergrowth is invariably replaced with symplectic clinopyroxene-plagioclase or a rind of plagioclase. Textural modeling of the reaction textures and mineral compositions suggests that the garnet-titanite became unstable and the ilmenite-clinopyroxene preferentially develop after titanite. The presence and texture of halogen rich apatite within the ilmenite-clinopyroxene are consistent with a fluid mediated process. Thermodynamic modeling in the NCFMAST (+$H_2O$) system, demonstrates that the clinopyroxene-ilmenite symplectite was formed along a steeply decompressive retrograde P-T path (from ~13 kbar to ~7 kbar, at ~800°C), in the presence of partial melts. The study demonstrates that relative to Fe, Mg, and Ca, Ti was less mobile and that the mobility of Ti was restricted within the confines of titanite being replaced by the clinopyroxene-ilmenite symplectite. This study implies that besides the ligand activity, the fluid/rock ratio exerts a strong control on the length scale of Ti transport in natural rocks.

**Keywords:**

**Clinopyroxene-ilmenite symplectite; High pressure metamorphisim; CGGC; Textural modeling; CSpace; XMapTools; Ti mobility.**

## INTRODUCTION

Symplectic intergrowths of clinopyroxene and ilmenite are quite rare in metamorphic rocks. Clinopyroxene-ilmenite symplectites have been reported from mantle xenolith of deep origin, kimberlites, and other alkaline rocks (Nixon and Boyd 1979; Garrison and Taylor 1981; Litasov

et al. 2003; Ashchepkov et al. 2014 and the references therein), where, their origin is explained either by exsolution from high pressure garnet (Ringwood and Lovering 1970) or clinopyroxene (Dawson and Reid 1970), or by cotectic or eutectic co-precipitation from a protokimberlite melt (Nixon and Boyd 1979; Garrison and Taylor 1981; Litasov et al. 2003). But in metamorphic rocks formation of clinopyroxene-ilmenite symplectites is even rarer, and its occurrence is mainly restricted to high pressure metamorphic rocks such as HP basic granulites and retrogressed eclogites (O'Brien and Rötzler 2003; Zhang et al. 2003; Faryad et al. 2006; Marsh and Kelly 2017). Depending upon bulk rock compositions and the ambient physiochemical conditions, metabasic rocks contain one or more of the accessory phases, like titanite, rutile, and ilmenite that chiefly contribute to the Ti-budget of the metabasic rocks. Experimental studies have shown that the solubility of Ti in pure $H_2O$ is very low over a range of pressure and temperature (nominally soluble, Purtov and Kotel'nikova 1993; Ryzhenko et al. 2006; Antignano and Manning 2008; Rapp et al. 2010; Hayden and Manning 2011; Tanis et al. 2016; Karmakar 2021). However, the solubility of Ti is dramatically enhanced in presence of halogen-rich, particularlyF-rich fluid (Rapp et al.2010). The experimental data suggest, therefore, different length scale of transport of Ti in crustal rocks depending on the physical conditions and the composition of the transporting media (Antignano and Manning 2008; Rapp et al. 2010; Hayden and Manning 2011). Furthermore, rutile, titanite, and ilmenite, the main Ti-sink of metabasic rocks, An understanding of the relative stability of the three Ti-rich phases put important constraints on the behavior of Tiduring the evolution of the metabasic rocks. Ti (and other HFSEs) is commonly used as a fixed reference frame for mass-balance calculations and geochemical interpretations in metamorphic and metasomatic processes (Ague 2011). This approach may be seriously affected if Ti becomes significantly mobile.

In this communication, we document an occurrence of clinopyroxene-ilmenite symplectite that grew after titanite in a suite of high pressure high temperature mafic granulites from the Chotanagpur Granite Gneissic Complex (CGGC), Eastern Indian Shield (Fig. 1a). Our study demonstrates that the clinopyroxene-ilmenite symplectite was formed due to the instability of garnet and titanite when the rock evolved along a steeply decompressive P-T path. Despite the presence of halogen-bearing fluid, the length scale of movement of Ti is restricted to a few tens of microns in length. The likely mechanism of formation of the clinopyroxene-ilmenite symplectite vis-à-vis the significance of the limited transport of Ti in the metamorphic regime is discussed.

## BACKGROUND GEOLOGY AND FIELD OBSERVATIONS

The CGGC comprises the northern part of the East Indian shield along with the southern Archean Singhbhum Craton, separated by the Proterozoic North Singhbhum Fold Belt (Fig. 1a). To the west of CGGC, occurs the Paleo to Neoproterozoic rocks of the Central Indian Tectonic Zone but its contact with CGGC is concealed by Gondwana sediments (Fig.1a). The northern and eastern boundaries of the CGGC are covered by sediments from Gangetic alluvium. On the basis of lithological, petrological, and geochronological data, CGGC is divided into three domains (Domain I, Domain II, and Domain III) by Mukherjee et al. (2019). These domains (Fig. 1a), trend approximately E-W. The southernmost Domain I records the most thorough geological history. Domain I is dominated by felsic orthogneiss, which contains a variety of mafic, metapelitic, and meta-calcareous enclaves.

Geological and geochronological data of Domain I reveal three distinct phases of deformation and metamorphism. These three metamorphic events were punctuated by several

mafic (Mukherjee et al. 2018b; Dey et al. 2019), felsic (Mukherjee et al. 2017, 2018a), anorthosite(Chatterjee et al. 2008), and alkaline (Das et al. 2018) magmatic events.

The earliest distinct metamorphic event ($D_1$-$M_1$) reached high to ultra-high temperature metamorphism between 1680-1580 Ma (Sanyal and Sengupta 2012; Dey et al. 2020). The most ubiquitous tectonothermal event ($D_2$-$M_2$), present throughout Domain I, is characterized by HP metamorphism with a decompressive retrograde P-T path (~12-9 kbar, 780-800°C) during the early Neoproterozoic (1000 - 950 Ma) time in an inferred continent-continent collisional setting (Chatterjee et al. 2008; Chatterjee and Ghose 2011; Karmakar et al. 2011; Rekha et al. 2011; Mukherjee et al. 2017; Dey et al. 2019, 2020). Between $D_1$-$M_1$and $D_2$-$M_2$ there was a pronounced period of felsic(1450 Ma) (Mukherjee et al. 2018a) and anorthosite (1550 Ma)(Chatterjee et al. 2008) magmatism. The subsequent $D_3$-$M_3$ event at 900-880 Ma deformed and metamorphosed the rocks at amphibole facies (Das et al. 2018; Mukherjee et al. 2018b) condition. These two metamorphic events were interrupted by some mafic (950-900 Ma) (Mukherjee et al. 2018b) and alkaline (Das et al. 2018) magmatism in CGGC.

The studied area belongs to the eastern margin of the CGGC, located to the northeast of the Masanjore dam site near Asanbani within Domain I. Like the rest of the CGGC Domain I, the country rock of the area comprises a variety of felsic orthogneiss, within which, the studied mafic granulites occur as subcrops along a NE-SW trend (Fig. 1b).

The mafic granulites are medium to coarse-grained, showing a distinct bimodal variation in grain size, and hence the mineralogy is quite evident from the outcrops scale. The medium-grained rock comprises garnet, clinopyroxene, plagioclase, and amphibole(Fig. 1c). The uniform distribution of garnet porphyroblasts (≤1cm diameter) imparts a spotted appearance to the rock (Fig. 1c). The coarse-grained part of the rock occur mostly as amoeboid patches or segregations

comprising plagioclase, garnet, amphibole, quartz, ± clinopyroxene(Fig. 1d). The patches have a rim of amphibole around them, separating them from the medium-grained host rock, the boundary between the two being gradational (Fig. 1d). These patches possibly represent segregated partial melts or leucosomes.

## PETROGRAPHY

The studied rocks display plethora of textures that presumably formed in response to the changing physicochemical conditions the rock traversed. In the following section, the textures that help understand the formation of the ilmenite-clinopyroxene intergrowth are discussed. Based on overprinting relations, textures and mineralogy of the studied rock can be divided into primary and secondary. The primary textures are defined by the granoblastic aggregates of garnet, clinopyroxene ($Cpx_1$), plagioclase ($Pl_1$), and rare quartz (Fig.2a-b). Titanite and rutile (Fig. 2f-g; 3a-b) that occur as accessory phases are scattered in the granoblastic mosaic. Garnet grains of variable size (1 mm to ≤10 mm) and shape contain one or more of the inclusions quartz, plagioclase ($Pl_0$), and amphibole ($Amp_0$) (Fig. 2c), rutile, and ilmenite. Rarely, garnet contains ilmenite inclusion that is successively rimmed by rutile and plagioclase (Fig. 2e). Although the inclusion of titanite is not seen in garnet, locally inclusion of titanite is seen within the granoblastic clinopyroxene ($Cpx_1$) getting replaced by amphibole ($Amp_2$) (Fig. 2g). This raises the possibility that titanite and rutile were stabilized during and/or prior to the stabilization of the granoblastic assemblage. Locally inclusion of amphibole ($Amp_0$) and plagioclase ($Pl_0$) occur within $Cpx_1$ (Fig. 2d). The secondary textures are formed after the primary granoblastic assemblage. The most conspicuous secondary texture is a fine symplectic intergrowth of ilmenite and clinopyroxene ($Cpx_2$) (<2µm to 55µm lamellar width). The Ilm-$Cpx_2$ symplectite variably replaces titanite (Fig. 3a-f, 4d-h). The Ilm-$Cpx_2$ symplectite has a bulbous/wavy front that

protrudes into the titanite (Fig. 3a-b). Locally the Ilm-$Cpx_2$ symplectite completely replaces titanite preserving the original boundary of the titanite it replaces (Fig. 3c-d). Ilmenite in the central part of the Ilm-$Cpx_2$ symplectite form fine rod-shaped lamellae with small inter lamellar space (~2µm, Fig.3d). Marginal part of the symplectite show distinctly coarse and irregular ilmenite lamellae in the matrix of clinopyroxene ($Cpx_2$) (Fig. 3d). The Ilm-$Cpx_2$ symplectite contains fine grains of apatite (mostly visible in the Ca- X-ray intensity maps as the fine red dots within the symplectic domain) (Fig. 4g; 5g). Rarely, small volume of orthopyroxene lamellae are seen in ilmenite-clinopyroxene ($Cpx_2$) symplectite (Fig. 4d). The Ilm-$Cpx_2$ symplectite is separated from garnet by a rind of plagioclase ($Pl_2$) (Fig.3c) or a symplectic intergrowth of plagioclase ($Pl_2$) and clinopyroxene ($Cpx_2$) that protrudes into garnet (Fig. 3d-e). Proximal to titanite, Ilm-$Cpx_2$ symplectite (Fig. 3a-b;e) develops that commonly replaces the titanite completely (Fig.3c-d). Nowhere in the rock does Ilm-$Cpx_2$ symplectite show physical contact with garnet. Plagioclase rind or $Pl_2$-$Cpx_2$ symplectite is always proximal to the garnet grain boundary. So, the secondary clinopyroxene ($Cpx_2$) is forming symplectic intergrowth with both plagioclase and ilmenite, from here on they are denoted as $Cpx_2^{PL}$ and $Cpx_2^{ILM}$ respectively. Secondary amphibole ($Amp_2$) variably replaces the primary granoblastic garnet, clinopyroxene (Fig. 2c; g-i). $Amp_2$ also replaces the secondary clinopyroxene ($Cpx_2$) (Fig.3e). This feature suggests that $Amp_2$ formed after the development of the secondary clinopyroxene ($Cpx_2$). Secondary amphibole ($Amp_2$) preserves the initial shape of the clinopyroxene when replacing $Cpx_1$ and $Cpx_2$ (pseudomorphic replacement) (Fig. 2i; 3e-f). During this replacement of $Cpx_1$, titanite inclusion appears to be stranded within the secondary phase ($Amp_2$) (Fig. 2g).

# PHASE COMPOSITION

## Analytical techniques

Major elemental analyses were performed using a Cameca SX100 Electron Probe Micro Analyser equipped with four wavelength-dispersive spectrometers (WDS) from the Department of Geology and Geophysics, Indian Institute of Technology, Kharagpur. All points were analyzed with 15 kV acceleration voltage, 20 nA beam current, and a beam size of 1 µm. The dwell time for the measured elements was set at 10 s for the peak and 5 s for the background. Natural minerals and synthetic compounds were used as standards.

Representative mineral compositions are presented in Tables 1 to 4. Mineral abbreviations in figures and tables have been used after (Whitney and Evans 2010). Cation recalculation for the estimation of $Fe^{3+}$ is done following the scheme of Droop (1987). In the following section, salient compositional features of the minerals are described.

## Mineral compositions

**Garnet.** The garnets are dominantly solid solutions of almandine, pyrope, and grossular, with a minor amount of spessartine (Table-1): almandine (43- 57mol %) contents are highest with a lesser amount of grossular (19- 33 mol%) and pyrope (16- 26%) and minor spessartine (1- 4 mol%). The porphyroblasts show internal core-rim zonation with the core compositions being less ferroan and grossular rich ($Grt_C$: $Alm_{43-47}Grs_{28-33}Prp_{21-26}Sps_{1-2}$; $X_{Mg}$=0.31-0.37) than rims ($Grt_R$: $Alm_{49-57}Grs_{20-26}Prp_{16-20}Sps_{2-4}$; $X_{Mg}$=0.23-0.29). $TiO_2$ content of garnet is negligible, below 0.25 wt%. Garnet core composition is flat and homogenous, extended up to the thin rim.

**Pyroxene.** Representative data of the pyroxenes are presented in Table 2. Both matrix clinopyroxenes ($Cpx_1$) and symplectic clinopyroxenes ($Cpx_2^{PL}$ and $Cpx_2^{ILM}$) represent diopside-hedenbergite solid solutions with $X_{Mg}$=0.72-0.83(Fig 3a). $Cpx_1$ has slightly higher Al (0.12-0.24

a.p.f.u) and Na (0.03-0.05 a.p.f.u) content than $Cpx_2^{PL}$ and $Cpx_2^{ILM}$ (Al=0.05-0.10 a.p.f.u; Na=0.02-0.03 a.p.f.u). $TiO_2$ content of $Cpx_1$ (0.137-0.628 wt%), as well as Cpx2 (0.069-0.536 wt%), is negligible. The orthopyroxenes in the symplectic intergrowths are magnesian with ($X_{Mg}$=0.55-0.58, Fig 4i.).

**Plagioclase.** Representative plagioclase compositions are given in Table 3. There is a considerable variation in plagioclase compositions depending on the textural types with $X_{OR}$<1. The matrix plagioclase ($Pl_1$)shows a prominent increase in anorthite content from the core ($X_{An}$=0.43-0.60) to the rim ($X_{An}$=0.75-0.86) (Fig 3b). Symplectic plagioclase ($Pl_2$) is similar to the rim of $Pl_1$ ($X_{An}$=0.72-0.86).

**Amphibole.** Representative compositions of the amphiboles are presented in Table 4. According to the (Leake et al. 1997) and (Leake et al. 2004) classification scheme, all the amphiboles are calcic. The amphibole inclusions in garnets ($Amp_0$) are mostly pargasitic in nature with $X_{Mg}$=0.62-0.70. The matrix amphibole ($Amp_1$) composition ranges between tschermakite and magnesio-hornblende with $X_{Mg}$=0.59-0.72.

**Accessory minerals.** Representative chemical compositions of the accessory phases are in Table 5. Ilmenite present in the clinopyroxene + plagioclase symplectite is nearly pure $FeTiO_3$. Rutile is present as a pure phase. Titanite is slightly aluminous (1.1-1.4 wt% $Al_2O_3$) with no F. Apatite has 1.657 wt% of F and 0.25 wt% of Cl.

## MODELING THE FORMATION OF $CPX_2$ + ILM SYMPLECTITES USING CSPACE AND XMAPTOOLS

### Textural modeling of Ilm-$Cpx_2$(±Opx) symplectite: a mass balance approach

The textural features, described above, suggest that the symplectic intergrowth of Ilm-$Cpx_2$ (with rare Opx) develops preferentially over the titanite. Rutile was present prior to the formation of the symplectite. It is also possible that the rutile might have been involved in some symplectite forming process. However, textural features support involvement of titanite in the formation of Ilm-$Cpx_2$ symplectite, while such features on account of rutile (e.g. presence of rutile in the vicinity of or in contact with Ilm-$Cpx_2$ symplectite) are absent. Accordingly, the textural modeling study was carried out using titanite as the only Ti-bearing reactant phase that was replaced by the Ilm-$Cpx_2$ (± Opx).

Mass balance calculations with the measured mineral compositions are a powerful technique to explain the observed mineralogy and the textural relations (Fisher 1989; Lang et al. 2004; Sengupta et al. 2004; Chowdhury et al. 2013). This approach returns stoichiometrically balanced chemical reactions involving the reactant and product phases and hence, provides vital clues about the mobility of the different chemical species in a given compositional space (Lang and Rice 1985; Fisher 1989; Lang et al. 2004; Sengupta et al. 2004, 2009; Sengupta and Dasgupta 2009; Chowdhury et al. 2013; Karmakar et al. 2017). The computer program CSpace (Torres-Roldan et al. 2000) has been employed for identifying stoichiometrically balanced chemical reaction(s) involving the measured compositions of the reactant and product phases. This algebraic analysis with Cspaceinvolves the singular value decomposition (SVD) of a compositional matrix **M** of **m** mineral phases in terms of **n** components (**M=m x n**) (Lang et al. 2004).The chemical species that are suspected to show mobility (e.g FeO, MgO, CaO, $Na_2O$, $TiO_2$, etc in this study) are considered as 'phases' in the computational matrix (Sengupta and Dasgupta 2009). A detailed discussion on the SVD method is presented in several studies (Lang et al. 2004; Sengupta et al. 2004; Sengupta and Dasgupta 2009; Chowdhury et al. 2013). In the

multi-component system with a number of mobile species, the CSpace programs can return several stoichiometrically balanced reactions for a set of reactant and product phases. Of these probable reactions, if more than one reaction is returned by the CSpace, the likely reaction will be chosen based on the following criteria:

1. The observed reactant and the product phases must lie on the opposite side of the reaction
2. The calculated and observed volume ratio of the Ilm-$Cpx_2$ in the symplectite must match

**Calculation of volume ratio of Ilm-$Cpx_2$ symplectite obtained from reactions:** The coefficients in the obtained balanced reactions are the molar proportions of the phases and the volumes of the necessary solid phases are calculated by multiplying the molar proportions by the molar volume of that phase. The molar volume of the phase is obtained using the computer program PERPLE_X (ver. 6.9.1) (Connolly 2005, 2009) with the thermodynamic data of Holland and Powell (2011). For a particular solid solution phase, the molar volume of the different end-members are calculated, at an average P-T condition of 800°C, 9 kbar, based on the constrained physical conditions of metamorphism (presented in the following section). The molar volume of the solid-solution phases, ($V^{SS}$) is then calculated using the following relation:

$$\mathbf{V_N}^{\mathbf{SS}} = (X_A \times V_A) + (X_B \times V_B)$$

where A and B are the two end members of the solid-solution phase N, V is the molar volume of that end member, and X is the mole fraction of the corresponding end member.

**Estimation of volume ratio of Ilm-$Cpx_2$ symplectite using XMapTools:** The volume proportion of Cpx and Ilm only from the $Cpx_2$-Ilm symplectic domain is estimated to check how well the modeled reaction product is correlating with the observed textures. We have taken this as a parameter as other phases such as Grt, Pl are formed or consumed in other concurrent reactions, and texturally they can't be attributed solely to the titanite breakdown reaction.Owing to the fine-grained nature of the $Cpx_2$-Ilm symplectites, estimation of observed volume proportion is difficult. For accurate estimation of the phase proportions of Cpx and Ilm in the symplectites, the software XMapTools (ver. 3.4.3) (Lanari et al. 2014, 2019) is used. In this process X-ray intensity maps of the elements, Si, Ti, Al, $Fe^{TOTAL+2}$, Mg, Na, Ca (Fig 5a-g) of the selected microdomains, produced using EPMA, are used to classify all the different phases accurately with the help of XMapTools and phase proportions of Cpx and Ilm are calculated only from the symplectic domain (Fig. 5h), omitting all other phases present.

**The choice of domains for the textural modeling study**

Two micro-domains viz. Domain I and Domain II are chosen for detailed textural analyses. In Domain I (Fig.3c), Ilm-$Cpx_2$ symplectite is separated from the porphyroblastic garnet by a rind of $Pl_2$. In Domain II, Ilm-$Cpx_2$ symplectite is separated from garnet by a symplectic intergrowth of $Cpx_2$-$Pl_2$(Fig 3d). Proximal to garnet, the fine symplectite of clinopyroxene ($Cpx_2^{PL}$) and plagioclase ($Pl_2^{CPX}$) develops on and variably replaces the garnet. Away from garnet, lamellar intergrowth of $Cpx_2$-Ilm develops after titanite.

In both of the domains, the core and rim of garnet are respectively treated as reactant and product phases. The mineral compositions that are used for textural modeling from both of these micro-domains (Domain I and II) are marked with the superscript 'MDI' and 'MDII' in the data tables (Table 1-5) respectively.

**Modeled reactions in Domain I:** If all the product phases between titanite and garnet are considered, the CSpace program returns the net reaction:

3.61 **Ttn** + 7.28 $\mathbf{Grt_C}$ + 5.21 **Qz** + 1.20 [$\mathbf{Na_2O}$]

$$= 3.56\ \mathbf{Ilm} + 4.07\ \mathbf{Cpx_2^{ILM}} + 5.08\ \mathbf{Pl_2} + 1.00[\mathbf{CaO}] + 3.33\ \mathbf{Grt_R} \qquad \textbf{(1)}$$

$\mathbf{\Delta V_{SOLID} = V_{PRODUCTS} - V_{REACTANTS} = +7.5\%}$; Cpx/Ilm =2.4 (observed Cpx/Ilm: 2.2)

This net reaction has two parts.

At the titanite end, the likely reaction is,

3.61 **Ttn** + 4.50 **Qz** + 4.60 [**FeO**] + 3.0 [**MgO**] + 0.1 [**CaO**] + 0.05 [$\mathbf{Na_2O}$]

$$= 3.56\ \mathbf{Ilm} + 4.07\ \mathbf{Cpx_2^{ILM}} \qquad \textbf{(1.a)}$$

At the garnet end, the likely reaction is,

7.28 $\mathbf{Grt_C}$ + 0.72 **Qz** + 1.15 [$\mathbf{Na_2O}$]

$$= 3.33\ \mathbf{Grt_R} + 5.08\ \mathbf{Pl_2^{CPX}} + 4.60\ [\mathbf{FeO}] + 3.0\ [\mathbf{MgO}] + 1.1\ [\mathbf{CaO}] \qquad \textbf{(1.b)}$$

**Modeled reactions in domain II:** If all the products are considered CSpace program produces the following net reaction,

3.25 **Ttn** + 14.44 $\mathbf{Grt_C}$ + 7.10 **Qz** + 0.60 [$\mathbf{Na_2O}$]+ 1.00 [**CaO**]

$$= 3.19\ \mathbf{Ilm} + 6.80\ \mathbf{Cpx_2}(Cpx_2^{PL}+Cpx_2^{ILM}) + 6.75\ \mathbf{Pl_2} + 8.40\ \mathbf{Grt_R} \qquad \textbf{(2)}$$

$\mathbf{\Delta V_{SOLID} = V_{PRODUCTS} - V_{REACTANTS} = +6.6\%}$; Cpx($Cpx_2^{PL}$+$Cpx_2^{ILM}$)/Ilm = 4.5;

Similar to Domain I, the net reaction of Domain II can be divided into two sub-reactions. The following is the reaction at the titanite end,

3.25**Ttn** + 2.78**Qz** + 3.68 [**FeO**] + 2.40 [**MgO**] + 0.025 [$\mathbf{Na_2O}$]

$$= 3.19\mathbf{Ilm} + 3.02\mathbf{Cpx_2^{ILM}} + 0.5[\mathbf{CaO}] \qquad \textbf{(2.a)}$$

Calculated volume ratio of $\mathbf{Cpx_2/Ilm}$, from reaction 2.a= **2.0**;(Observed Cpx/Ilm = 1.9)

The reaction at the garnet end,

$$14.44\mathbf{Grt_C} + 4.32\mathbf{Qz} + 1.5\,[\mathbf{CaO}] + 0.57\,[\mathbf{Na_2O}]$$
$$= 8.40\mathbf{Grt_R} + 3.78\,\mathbf{Cpx_2^{PL}} + 6.57\,\mathbf{Pl_2} + 3.68\,[\mathbf{FeO}] + 2.40\,[\mathbf{MgO}] \qquad \textbf{(2.b)}$$

From the calculated volume change and volume ratios, Domain II is very similar to Domain I, except for the addition of orthopyroxene as a product in it. The presence of minor amounts of orthopyroxene observed in the $Cpx_2$-Ilm symplectic domains may be accounted for, by the following mass-balanced reaction:

$$3.29\mathbf{Ttn} + 14.44\,\mathbf{Grt_C} + 7.10\,\mathbf{Qz} + 0.60\,\mathbf{Na_2O} + 1.00\,\mathbf{CaO}$$
$$= 3.26\mathbf{Ilm} + 6.80\,\mathbf{Cpx} + 0.1\,\mathbf{Opx} + 6.75\,\mathbf{Pl} + 8.40\,\mathbf{Grt_R} \qquad \textbf{(3)}$$

## PHYSICAL CONDITIONS OF METAMORPHISM

Detail study of the P-T evolution of the mafic rocks is beyond the purview of this study. In the following sections emphasis will be given to the reconstruction of the change in the physical conditions of metamorphism that led to the formation of the ilmenite-plagioclase–clinopyroxene intergrowth after the primary granoblastic assemblages.

### Choice of phase compositions for the estimation of P-T condition of metamorphism

Ubiquitous presence of the assemblage garnet-clinopyroxene-plagioclase-quartz-titanite (±rutile) suggests that the studied mafic granulites witnessed high pressure metamorphism(O'Brien and Rötzler 2003; Pattison 2003). The high pressure assemblage was presumably in equilibrium with a melt phase (represented by the garnet-bearing leucosome) at the thermal maxima. A number of studies have shown that high pressure metamorphism of the rocks of diverse bulk compositions develop garnet on the prograde path. These garnet grains may serve as a substrate over which new garnet rims grow till the $T_{max}$ (maximum temperature) is reached(Saxena and Ganguly

1987; Spear 1993). This leads to prograde growth zoning (rim-ward decrease in Fe and Mn and increase in Mg) in garnet (Harte and Henley 1966; Hollister 1966; Lopez Ruiz 1976; Tuccillo et al. 1990; Ikeda 1993; Nyström and Kriegsman 2003; Kohn 2014; Dempster et al. 2020). Since garnet preferentially partitions Fe relative to the coexisting pyroxene, the highest temperature will be obtained with rim compositions of garnet and coexisting pyroxene if the former shows growth zoning. X-ray intensity maps and the measured composition of garnet show distinct enrichment of Fe and Mn in the thin rim (30-80μm) relative to the core of garnet (Fig. 4a;4c). The core part of garnet is compositionally homogeneous and is Mg-rich relative to the thin rim (Fig.4d). The thin rim of garnet, therefore, is interpreted to have formed during the partial exchange of elements with the coexisting ferromagnesian phases during retrogression (Spear 1993). Studies have demonstrated that at temperature >750°C and in presence of a melt phase, volume diffusion in garnet and pyroxene are sufficiently fast to homogenize large garnet porphyroblasts (>0.5 mm)over a range of cooling rates(Chakraborty and Ganguly 1991; Carlson and Schwarze 1997; Ganguly et al. 1998; Chakraborty 2008; Caddick et al. 2010). Several studies in high temperature granulite metamorphic belts record that equilibrium among the mineral assemblages that developed during the $T_{max}$ occurs over a large area (several square km, Kelsey and Hand 2015). This explains the rare preservation of growth zoning in garnet in high to ultra-high temperature metamorphism. Rapid and short-lived heating at a high temperature can only develop the rare prograde zoning in high to ultra-high temperature granulites(Chen et al. 1998; Hollis et al. 2006). In view of all the observations, the compositionally homogeneous core compositions are chosen for the estimation of pressure and temperature during which the primary(granoblastic) assemblages equilibrated. The compositions of the symplectic minerals

and the rims of the porphyroblastic phases constrain the physical conditions during which the symplectic assemblage equilibrated during retrogression.

**Conventional thermobarometry**

For estimation of temperature, $Fe^{2+}$- Mg exchange thermometer involving garnet and clinopyroxene is used (Ellis and Green 1979). Metamorphic pressure has been computed from the assemblage garnet-plagioclase-clinopyroxene-quartz (GCPS, Eckert et al. 1991). The core compositions of the granoblastic assemblage of $Grt_C$+$Pl_1$+$Cpx_1$(±Qz), yield a tight cluster of temperature of 800-850°C (Table-6). The Fe-Mg exchange thermometer has a very steep slope in the P-T field. This together with the accuracy of the geothermometer (± 50°C) suggest that the choice of reference pressure should not affect the estimated temperature values. At the reference temperature of 850°C, the GCPS barometer yields 12-13 kbar pressure for the core compositions of the granoblastic (primary) phases. The temperature of 850°C is, therefore, considered to be the maximum temperature recorded by the primary assemblages at the estimated pressure of 13 kbar. The rim compositions of garnet ($Grt_R$) coupled with symplectic $Pl_2$+$Cpx_2^{PL}$ yield distinctly lower temperature (650-700°C) and pressure (6.5-8 kbar, Table-6). The estimated pressure and temperature is considered as the recorded physical conditions when the symplectic intergrowth of $Cpx_2$-$Pl_2$ and Ilm-$Cpx_2$ were formed.

**Isopleth intersection in pseudosection**

Notwithstanding the following points:

1. The numerically computed phase diagram (pseudosection) is influenced by the input bulk rock composition. The chosen bulk rock composition may or may not represent the composition of the equilibrium.

2. Uncertainties associated with the internally consistent thermodynamic data and the activities of the solid solutions

The isopleths intersection methods yield reasonably well constrained P-T estimate for metamorphism and are widely used by petrologists (Evans 2004; Palin et al. 2016).

The P-T pseudosection has been computed using the program Perple_X (ver. 6.9.1; Connolly 2005) with the internally consistent thermodynamic dataset of Holland and Powell 2011 (TC-DS633). The a-X relationships of the minerals chosen for the numerical calculations of the phase diagram are the following: clinopyroxene (Holland et al. 2018), clino-amphibole (Green et al. 2016), melt (Holland et al. 2018), garnet (Holland et al. 2018), orthopyroxene (Holland et al. 2018), feldspars (Holland and Powell 2003). The numerically computed phase diagram is presented in Figure 6a-c. In the computed P-T pseudosection, the primary granoblastic assemblage ($Grt_C$-$Pl_1$-$Cpx_1$-Qz-Ttn-Rt) coexists with a melt phase at temperature >800°C between 9-13 kbar (Fig.6a-b). The intersection of the isopleths of the garnet core ($X_{ALM}$, $X_{PRP}$, $X_{GRS}$) and the plagioclase ($X_{AN}$) define a narrow P-T domain of 800-900°C and 11-13 kbar (Fig. 6b). Several experimental studies on a range of basaltic compositions showed that dehydration melting of the basic rock produces high pressure assemblage (garnet+clinopyroxene+plagioclase+q) at >800°C between ~10-13 kbar (Rötzler and Romer 2001; Vielzeuf and Schmidt 2001; O'Brien and Rötzler 2003; Pattison 2003). The presence of abundant garnet-bearing leucosome, presumed to be a melt phase, with the primary granoblastic assemblage and the results of the melting experiment on mafic protolith corroborate the P-T values calculated of 800-900°C and 11-13 kbar from the isopleths intersection method. The computed P-T pseudosection has a small P-T field (7-9 kbar and ~750-800°C) in which the symplectic intergrowth of Ilm+$Cpx_2$(±Opx) and the plagioclase rind is stable with garnet. The

isopleths of garnet rim($X_{ALM}$, $X_{PRP}$, $X_{GRS}$) and the symplectic plagioclase ($Pl_2$; $X_{AN}$)converge within this field at ~7.5-8 kbar and 750-780°C (Fig. 6b).

## DISCUSSION

### Textural modeling of $Cpx_2$-Ilm symplectite: an algebraic approach

Textural features suggest that the garnet and titanite(±rutile)of the primary assemblages became unstable and are separated by two types of symplectites. The symplectite of Ilm-$Cpx_2$(±Opx) develops near and variably replaces the titanite. Whereas the symplectite of $Cpx_2$ + $Plg_2$ replaces garnet and forms away from the titanite (Fig. 3d-e). In another situation, a rind of plagioclase having the same compositions as in $Pl_2$ develops at the contact of and replaces garnet porphyroblasts (Fig. 3c). Rutile is found to coexist with garnet but not in the symplectite domains. This raises two possibilities. One likely scenario is that rutile might be consumed during the formation of the Ilm-$Cpx_2$ symplectite and preserved only where the symplectite did not form. While there exists clinching textural evidence in support of Ilm-$Cpx_2$ symplectite partially to completely replacing titanite, the role of rutile in the formation of this symplectite remains unclear. In the following section, we will focus on the process that promoted the growth of the Ilm-$Cpx_2$ and $Cpx_2$-$Plg_2$ symplectites after the primary titanite and garnet.

**Formation of symplectites: Solution-reprecipitation vs volume diffusion:** Two endmember processes, commonly working in tandem, are invoked to explain mineral replacement textures. These are (a) volume diffusion(Lasaga 1981; Ganguly 2002; Watson and Baxter 2007; Chakraborty 2008) and (b) solution reprecipitation(Putnis 2002, 2009; Hellmann et al. 2003; Putnis and Putnis 2007; Ruiz-Agudo et al. 2014). Though both processes can be driven by temperature, each process has its characteristic mechanism of mass transport during the mineral replacement. In the case of the diffusion-driven process, the framework of the mineral being

replaced remains essentially intact. Mass transport, through volume diffusion, occurs through the framework during the replacement process (Ganguly 2002; Chakraborty 2008). In the case of a fluid-aided solution and reprecipitation driven process, mineral replacement occurs through complete destruction of the reactant minerals, and the product phases are formed with new bonds (Putnis 2002, 2009). The replacement process can be isochemical or allochemical (common) depending on the composition of the fluid vis-à-vis the phases being replaced and the ambient physical condition(Putnis and Putnis 2007; Putnis 2009). A number of features suggest that the fluid-mediated solution-reprecipitation process dominated during the formation of Ilm-$Cpx_2$ symplectite after titanite (with or without rutile). These are:

1. Titanite has triclinic symmetry that is completely different from ilmenite (trigonal) and clinopyroxene (monoclinic). This then follows that the growth of Ilm-$Cpx_2$ symplectite requires complete breakdown of all the bonds in the titanite and redistribution of elements including Ti. The replacement also involves a marked change in chemistry as the reactant titanite contains insignificant FeO and MgO relative to Ilm-$Cpx_2$. These features are consistent with fluid aided solution-reprecipitation process (Putnis and Putnis 2007; Putnis 2009).
2. The original outline of the reactant titanite is conserved during the variable replacement of titanite by Ilm-$Cpx_2$ symplectite (pseudomorphic replacement, Fig.3c-d). Several studies have demonstrated that pseudomorphic mineral replacement texture is the consequence of the fluid-mediated solution reprecipitation process in which replacement occurs in nano- to micrometer scale at nearly(Putnis 2009; Ruiz-Agudo et al. 2014). The wavy/ bulbous outline of the protruding Ilm-$Cpx_2$front into the titanite (Fig. 3a-b) also supports the solution-reprecipitation process.

3. The Ilm-$Cpx_2$ symplectite contains tiny apatite with significant F and Cl. Since the primary assemblage does not have any sink of P or the halogens, only a fluid-mediated process can explain the texture.
4. The Ilm-$Cpx_2$ symplectite is commonly associated with $Pl_2$-$Cpx_2$symplectite that preferentially replaces garnet porphyroblasts. Plagioclase in the symplectite contains a significant albite molecule (Ab 15-25%). Since the garnet composition cannot account for the Na in the symplectic plagioclase, Na must be supplied by the fluid.

**Mobility of chemical species during the formation of Ilm-$Cpx_2$ symplectite:** The mass-balanced reactions (Reaction 1-2) that are obtained from textural modeling studies suggest the mobility of a number of chemical species across the initial boundary between garnet and titanite. In Domain I wherein $Cpx_2$ did not develop with $Pl_2$, the breakdown of garnet to plagioclase rind releases FeO, MgO, and CaO by the reaction (1.b)(Fig.7a). These chemical species moved to and reacted with the titanite by a fluid-mediated process to produce Ilm-$Cpx_2$ by reaction (1.a)(Fig.7a). This feedback mechanism can explain the complete and partial decomposition of titanite and garnet respectively in Domain I (Fig.7a). Both reactions (1.a-b) consumes $Na_2O$. Furthermore, F, Cl-bearing apatite formed as a part of the Ilm-$Cpx_2$ symplectite. These observations require that the infiltrated fluid also supplied $P_2O_5$, $Na_2O$, and halogens.

Similar feedback mechanism seems to have prevailed in Domain II as well where $Cpx_2$-$Pl_2$ symplectite formed after garnet (Fig.7b). However, in contrast to Domain I, CaO in Domain II moved from the titanite end (now completely replaced with Ilm-$Cpx_2$-Opx intergrowth) to the garnet end (Fig.7b). Since quartz is present in the rock, it is presumed that the symplectite forming reactions consumed the quartz in domains I and II.

X-ray intensity map of Ti (Fig.4h; 5c) and the modeled symplectite forming reactions in both domains suggest that Ti was not mobile beyond the volume of the initial titanite grain. However, the lamellar intergrowth of Ilm-$Cpx_2$ does support that Ti was locally mobile in the scale defined by the interlamellar space(Abart et al. 2012; Remmert et al. 2018) between Ilm lamellae. The interlamellar space between the lamellar ilmenite rods ranges from ~2-55μm in Domains I and II. Coarsening of the fine rods of ilmenite to bigger lamellae further attest to the view that Ti was indeed mobile but its length scale of mobility was much smaller than the mobility of FeO, MgO, and CaO (Fig.7a-b). The length scale of mobility of the latter species covered the whole width of the product phases that develop between titanite and garnet (Fig.7a-b). Owing to the smaller size of the titanite (than garnet) and the length scale of the transport of FeO, MgO, and CaO completely replaced the titanite with the Ilm-$Cpx_2$ (±Opx) symplectite in both Domains I and II. The solubility of $TiO_2$ is low in pure $H_2O$ or even in alkali, silica-bearing hydrous fluids (Audétat and Keppler 2005; Tropper and Manning 2005; Antignano and Manning 2008; Lucassen et al. 2010; Hayden and Manning 2011), However, the presence of halogens can significantly enhance the solubility of $TiO_2$ in the aqueous fluids (Purtov and Kotel'nikova 1993; Ryzhenko et al. 2006; Antignano and Manning 2008; Rapp et al. 2010; Hayden and Manning 2011; Tanis et al. 2016; Karmakar 2021). The presence of significant F and Cl in apatite granules in Ilm-$Cpx_2$ symplectite support the view that segregations of ilmenite in the Ilm-$Cpx_2$(±Opx) symplectites were formed in presence of a halogen-bearing fluid. This fluid helped the migration of Ti in the length scale of the interlamellar space of the Ilm rods (Abart et al. 2012; Remmert et al. 2018). Very low concentrations of halogen in secondary amphibole that replaced the Ilm-$Cpx_2$ symplectite can be explained by the greater affinity of halogens in apatite structure relative to amphibole. The Ti content of amphibole is higher than the two minerals (Cpx and garnet) that it

extensively replaces (Fig. 4h, 5c) and textural features (2f-g; 3e-f) suggest any one or all of the Ti-bearing accessory phases can be responsible.

**Formation of Ilm-Cpx$_2$: the control of metamorphic P-T path**

The foregoing analyses (Physical condition of metamorphism) suggest that different methods of P-T calculations suggest that the primary granoblastic assemblages (including both titanite and rutile) were formed in the realm of high pressure and high temperature (800-850°C and 12-14 kbar; Table-6, Fig. 6b) in the presence of partial melt. Studies have shown that melting and accompanying thermal maxima ($T_{max}$) in the high- to ultrahigh-pressure metamorphism can occur at a pressure that is significantly lower than the $P_{max}$ (maximum pressure). The phenomenon of "decompression melting" has been documented from several areas (Groppo et al. 2012; Chen et al. 2017; Deng et al. 2018; Liu and Massonne 2022). It is, therefore, difficult to identify if the pressure of 12-13 kbar represents the $P_{max}$ or the primary granoblastic assemblage achieved this pressure during decompression and melting(Fig. 6b). High temperature metamorphism in the studied area homogenized the primary porphyroblastic phases. However, the presence of amphibole(Amp$_0$) and plagioclase (Pl$_0$) as inclusion phases in garnet and clinopyroxene (Cpx$_1$) suggests the dehydration melting reaction,

$$Amp_1 + Pl_0 \rightarrow Grt_c + Cpx_1 \pm Qz + melt \qquad (4)$$

This reaction has been inferred to explain the formation of mafic migmatites during high pressure and temperature metamorphism (Vielzeuf and Schmidt 2001; Pattison 2003; Watkins et al. 2007).

If the estimated P-T values of the primary granoblastic assemblage and the Ilm-Cpx$_2$ symplectite are joined, a steeply decompressive retrogressed P-T path results (Fig.6b). The volume increase (6.5-7.5 %) that is predicted by the texturally modeled chemical reactions (Reaction 1-2) is

consistent with the view that the Ilm-$Cpx_2$ were formed on the steeply decompressive retrograde P-T path. Though the textural modeling was done with titanite in the chosen microdomains, rutile could also participate in other symplectic domains that are not studied here. The computed pseudosection shows the presence of a melt phase even when the symplectites were formed (Fig.6b). Based on textural evidence and the computed phase diagram, it seems likely that the secondary amphibole formed after the formation of the clinopyroxene bearing symplectite presumably during cooling. Incomplete hydration of the granulite facies assemblage could be governed by several factors including ease of fluid movement and the abeyant physical conditions.

## IMPLICATIONS

Understanding the factors that control the stability of titanite over ilmenite and rutile is crucial for the reconstruction of the tectonic history of the rocks in orogenic belts (cf.Angiboust and Harlov 2017; Zhou et al. 2021). Experimental studies in rocks of mafic (Liou et al. 1998) and felsic compositions (Angiboust and Harlov 2017) demonstrated that at higher pressure (>7 kbar) ilmenite is unstable and is transformed into titanite and/or rutile. Liou et al (1998) demonstrated that in the basaltic system, titanite becomes unstable in favor of rutile at the pressure interval of 14-16 kbar in the temperature range of 600°-1000°C. The observation of Liou et al.(1998) was also corroborated by Angiboust and Harlov (2017). Between 7-16 kbar the relative stability of rutile over titanite is strongly affected by several chemical factors in which the activity of CaO is the most dominating factor (Liou et al. 1998; Frost et al. 2001; Angiboust and Harlov 2017). Our study has demonstrated that titanite (with or without rutile) can be stable in mafic rocks beyond 17 kbar at a temperature ≥1000°C (Fig.6). This observation is consistent with the occurrence of titanite in high-pressure mafic granulites where pressure exceeded 22 kbar (Romer and Rötzler

2003; Rötzler et al. 2004). Therefore, the presence of titanite, in exclusion of rutile, in mafic and felsic granulites should not be taken as *prima facie* evidence for the absence of high-pressure metamorphism or formation of titanite from rutile during exhumation of high-pressure rocks as suggested in some studies (cf. Angiboust and Harlov 2017). The absence of zircon or baddyelite often poses a constraint in fixing the timing of high pressure metamorphism in mafic rock (cf. Timmerman 2004). U-Pb dating of titanite can be a useful technique for constraining the age of high-pressure metamorphism if titanite develops at the peak metamorphic pressure as has been documented here (Romer and Rötzler 2003; Timmerman 2004; Scibiorski et al. 2019; Zhou et al. 2021). A number of experimental investigations and studies in metasomatic rocks have demonstrated that the solubility of Ti and other High Field Strength Elements (HFSE) can be greatly enhanced in aqueous fluids due to the formation of ligands involving F, Cl, $PO_4^{2}$, $SO_4^{2}$, $CO_3^{2,-}$(Ryzhenko et al. 2006; Antignano and Manning 2008; Rapp et al. 2010; Hayden and Manning 2011; Tanis et al. 2016; Borovikov et al. 2017; Liu et al. 2022). A reduction of ligand activities, therefore, facilitates the deposition of the HFSE-bearing minerals (Gieré 1992). It is likely that the formation of the tiny apatite grains rich F (~1.66wt%) and Cl (~0.25 wt%) in the Ilm-$Cpx_2$ symplectite reduced the ligand activities and, therefore, facilitated the deposition of ilmenite during decompression. Precipitation of Ti-bearing phases due to reduced ligand activities have been reported (Gieré 1986, 1992; Gao et al. 2007; Rapp et al. 2010; Xiao et al. 2021). This study also demonstrates that both CaO and FeO activities, besides lowering of pressure, play a critical role in the replacement of titanite with ilmenite. Precipitation of CaO-bearing phases (e.g. clinopyroxene), reduced CaO activity whereas break down of garnet, enhanced FeO activity in that helped titanite-ilmenite transition in the reaction domains. The presence of hydrothermal veins rich in Ti-bearing minerals at different crustal depths requires

long transport of Ti by hydrothermal/metamorphic fluids in the scale of more than 1 meter to a km or more (Gieré 1992; Gao et al. 2007; Rapp et al. 2010; Borovikov et al. 2017; Xiao et al. 2021). In the present study, fluid-aided mobility of Ti is shown to be restricted within a few tens of microns of the reactant titanite (the length scale of ilmenite-clinopyroxene intergrowth). It is also demonstrated that the activities of CaO and FeO in the ambient fluid phase were buffered by local mineral reactions during the formation of the ilmenite-clinopyroxene symplectite. Two major factors seem to be responsible for the smaller transport of Ti in the studied rocks. These are (1) fluid flow was not pervasive (low fluid/rock ratio) enough to destroy the buffering capacity of rocks and hence could not promote long transport of Ti as seen in Ti-bearing mineral veins and (2) reduction of F, Cl and CaO in fluid due precipitation of F, Cl bearing apatite and $Cpx_2$ further restricted the long transport of Ti. Restricted hydration of the granulite facies assemblages during decompression and cooling is consistent with a low fluid-rock ratio. Our study stresses the need for detailed petrological analyses before using Ti as a reference frame for the estimation of element mobility of chemically altered rocks.

## ACKNOWLEDGEMENTS

S.C. acknowledges the financial support from the Council of Scientific and Industrial Research (CSIR fellowship scheme at Department of Geology, Jadavpur University,Kolkata). S.M. acknowledges the grant received from Department of Science and Technology under DST-INSPIRE Faculty scheme at Department of Geology, University of Delhi. P.S. and S.S. are thankful to DST-PURSE, DST-FIST and CAS-Phase-VI, obtained by Department of Geological Sciences, Jadavpur University. PS acknowledges the AvH Foundation for a fellowship during which the final ms was prepared. We express our sincere gratitudes to the two anonymous

reviewers for their constructive comments, which immensely helped us improve the manuscript. We also thank Professor Baker for his editorial work.

## REFERENCES

Abart, R., Petrishcheva, E., and Joachim, B. (2012) Thermodynamic model for growth of reaction rims with lamellar microstructure. American Mineralogist, 97, 231–240.

Ague, J.J. (2011) Extreme channelization of fluid and the problem of element mobility during Barrovian metamorphism. American Mineralogist, 96, 333–352.

Angiboust, S., and Harlov, D. (2017) Ilmenite breakdown and rutile-titanite stability in metagranitoids: Natural observations and experimental results. American Mineralogist, 102, 1696–1708.

Antignano, A., and Manning, C.E. (2008) Rutile solubility in H2O, H2O-SiO2, and H2O-NaAlSi3O8 fluids at 0.7-2.0 GPa and 700-1000 °C: Implications for mobility of nominally insoluble elements. Chemical Geology, 255, 283–293.

Ashchepkov, I. V., Alymova, N. V., Logvinova, A.M., Vladykin, N. V., Kuligin, S.S., Mityukhin, S.I., Downes, H., Stegnitsky, Y.B., Prokopiev, S.A., Salikhov, R.F., and others (2014) Picroilmenites in Yakutian kimberlites: Variations and genetic models. Solid Earth, 5, 915–938.

Audétat, A., and Keppler, H. (2005) Solubility of rutile in subduction zone fluids, as determined by experiments in the hydrothermal diamond anvil cell. Earth and Planetary Science Letters, 232, 393–402.

Borovikov, A.A., Vladykin, N. V, Tretiakova, I.G., and Dokuchits, E.Y. (2017) Physicochemical conditions of formation of hydrothermal titanium mineralization on the Murunskiy alkaline massif, western Aldan (Russia). Ore Geology Reviews, 95, 1066–1075.

Caddick, M.J., Konopásek, J., and Thompson, A.B. (2010) Preservation of garnet growth zoning and the duration of prograde metamorphism. Journal of Petrology, 51, 2327–2347.

Carlson , W.D., and Schwarze, E. (1997) Petrological significance of prograde homogenization of growth zoning in garnet: an example from the Llano Uplift. Journal of Metamorphic Geology, 15, 631–644.

Chakraborty, S. (2008) Diffusion in solid silicates: A tool to track timescales of processes comes of age. Annual Review of Earth and Planetary Sciences, 36, 153–190.

Chakraborty, S., and Ganguly, Jibamitra (1991) Compositional Zoning and Cation Diffusion in Garnets. In J Ganguly, Ed., Diffusion, Atomic Ordering, and Mass Transport: Selected Topics in Geochemistry pp. 120–175. Springer US, New York, NY.

Chatterjee, N., and Ghose, N.C. (2011) Extensive Early Neoproterozoic high-grade metamorphism in North Chotanagpur Gneissic Complex of the Central Indian Tectonic Zone. Gondwana Research, 20, 362–379.

Chatterjee, N., Crowley, J.L., and Ghose, N.C. (2008) Geochronology of the 1.55 Ga Bengal anorthosite and Grenvillian metamorphism in the Chotanagpur gneissic complex, eastern India. Precambrian Research, 161, 303–316.

CHEN, N., Sun, M., YOU, Z., and Malpas, J. (1998) Well-preserved garnet growth zoning in granulite from the Dabie Mountains, central China. Journal of Metamorphic Geology, 16, 213–222.

Chen, Y.X., Zhou, K., and Gao, X.Y. (2017) Partial melting of ultrahigh-pressure metamorphic rocks during continental collision: Evidence, time, mechanism, and effect. Journal of Asian Earth Sciences, 145, 177–191.

Chowdhury, P., Talukdar, M., Sengupta, P., Sanyal, S., and Mukhopadhyay, D. (2013) Controls

of P-T path and element mobility on the formation of corundum pseudomorphs in Paleoproterozoic high-pressure anorthosite from Sittampundi, Tamil Nadu, India. American Mineralogist, 98, 1725–1737.

Connolly, J.A.D. (2005) Computation of phase equilibria by linear programming: A tool for geodynamic modeling and its application to subduction zone decarbonation. Earth and Planetary Science Letters, 236, 524–541.

Connolly, J.A.D. (2009) The geodynamic equation of state: What and how. Geochemistry, Geophysics, Geosystems, 10.

Das, S., Sanyal, S., Karmakar, S., Sengupta, S., and Sengupta, P. (2018) Do the deformed alkaline rocks always serve as a marker of continental suture zone ? A case study from parts of the Chotanagpur Granite Gneissic complex , India. Journal of Geodynamics, 1–21.

Dawson, J.B., and Reid, A.M. (1970) A pyroxene-ilmenite intergrowth from the Monastery Mine, South Africa. Contributions to Mineralogy and Petrology, 26, 296–301.

Dempster, T.J., Coleman, S., Kennedy, R., Chung, P., and Brown, R.W. (2020) Growth zoning of garnet porphyroblasts: Grain boundary and microtopographic controls. Journal of Metamorphic Geology, 38, 1011–1027.

Deng, L.P., Liu, Y.C., Gu, X.F., Groppo, C., and Rolfo, F. (2018) Partial melting of ultrahigh-pressure metamorphic rocks at convergent continental margins: Evidences, melt compositions and physical effects. Geoscience Frontiers, 9, 1229–1242.

Dey, A., Karmakar, S., Mukherjee, S., Sanyal, S., Dutta, U., and Sengupta, P. (2019) High pressure metamorphism of mafic granulites from the Chotanagpur Granite Gneiss Complex, India: Evidence for collisional tectonics during assembly of Rodinia. Journal of Geodynamics, 129, 24–43.

Dey, A., Karmakar, S., Ibanez-Mejia, M., Mukherjee, S., Sanyal, S., and Sengupta, P. (2020) Petrology and geochronology of a suite of pelitic granulites from parts of the Chotanagpur Granite Gneiss Complex , eastern India : Evidence for Stenian - Tonian reworking of a late Paleoproterozoic crust. Geological Journal, 55, 2851–2880.

Droop, G.T.R. (1987) A general equation for estimating Fe 3+ concentrations in ferromagnesian silicates and oxides from microprobe analyses, using stoichiometric criteria . Mineralogical Magazine, 51, 431–435.

Eckert, J.O., Newton, R.C., and Kleppa, O.J. (1991) The ΔH of reaction and recalibration of garnet-pyroxene- plagioclase-quartz geobarometers in the CMAS system by solution calorimetry. American Mineralogist, 76, 148–160.

Ellis, D.J., and Green, D.H. (1979) An experimental study of the effect of Ca upon garnet-clinopyroxene Fe-Mg exchange equilibria. Contributions to Mineralogy and Petrology, 71, 13–22.

Evans, T.P. (2004) A method for calculating effective bulk composition modification due to crystal fractionation in garnet-bearing schist: Implications for isopleth thermobarometry. Journal of Metamorphic Geology, 22, 547–557.

Faryad, S.W., Perraki, M., and Vrána, S. (2006) P-T evolution and reaction textures in retrogressed eclogites from Svetlik, the Moldanubian Zone (Czech Republic). Mineralogy and Petrology, 88, 297–319.

Fisher, G.W. (1989) Matrix analysis of metamorphic mineral assemblages and reactions. Contributions to Mineralogy and Petrology, 102, 69–77.

Frost, B.R., Chamberlain, K.R., and Schumacher, J.C. (2001) Sphene (titanite): Phase relations and role as a geochronometer. Chemical Geology, 172, 131–148.

Ganguly, J. (2002) Diffusion kinetics in minerals: Principles and applications to tectono-metamorphic processes. European Mineralogical Union Notes in Mineralogy, 4, 271–309.

Ganguly, J., Cheng, W., and Chakraborty, S. (1998) Cation diffusion in aluminosilicate garnets: Experimental determination in pyrope-almandine diffusion couples. Contributions to Mineralogy and Petrology, 131, 171–180.

Gao, J., John, T., Klemd, R., and Xiang, X. (2007) Mobilization of Ti – Nb – Ta during subduction : Evidence from rutile-bearing dehydration segregations and veins hosted in eclogite , Tianshan , NW China. Geochimica et Cosmochimica Acta, 71, 4974–4996.

Garrison, J.R., and Taylor, L.A. (1981) Petrogenesis of pyroxene-oxide intergrowths from kimberlite and cumulate rocks: co-precipitation or exsolution? American Mineralogist, 66, 723–740.

Gieré, R. (1986) Zirconolite, allanite and hoegbomite in a marble skarn from the Bergell contact aureole: implications for mobility of Ti, Zr and REE. Contributions to Mineralogy and Petrology, 93, 459–470.

——— (1992) Compositional Variation of Metasomatic Titanite from Adamello ( Italy ). Schweizerische mineralogische und petrographische Mitteilungen, 72, 167–177.

Green, E.C.R., White, R.W., Diener, J.F.A., Powell, R., Holland, T.J.B., and Palin, R.M. (2016) Activity–composition relations for the calculation of partial melting equilibria in metabasic rocks. Journal of Metamorphic Geology, 34, 845–869.

Groppo, C., Rolfo, F., and Indares, A. (2012) Partial melting in the higher Himalayan crystallines of Eastern Nepal: The effect of decompression and implications for the “channel flow” model. Journal of Petrology, 53, 1057–1088.

Harte, B., and Henley, K.J. (1966) Occurrence of compositionally zoned almanditic garnets in

regionally metamorphosed. Nature, 210, 689–692.

Hayden, L.A., and Manning, C.E. (2011) Rutile solubility in supercritical NaAlSi3O8-H2O fluids. Chemical Geology, 284, 74–81.

Hellmann, R., Penisson, J.M., Hervig, R.L., Thomassin, J.H., and Abrioux, M.F. (2003) An EFTEM/HRTEM high-resolution study of the near surface of labradorite feldspar altered at acid pH: Evidence for interfacial dissolution-reprecipitation. Physics and Chemistry of Minerals, 30, 192–197.

Holland, T., and Powell, R. (2003) Activity-compositions relations for phases in petrological calculations: An asymetric multicomponent formulation. Contributions to Mineralogy and Petrology, 145, 492–501.

Holland, T.J.B., and Powell, R. (2011) An improved and extended internally consistent thermodynamic dataset for phases of petrological interest, involving a new equation of state for solids. Journal of Metamorphic Geology, 29, 333–383.

Holland, T.J.B., Green, E.C.R., and Powell, R. (2018) Melting of peridotites through to granites: A simple thermodynamic model in the system KNCFMASHTOCr. Journal of Petrology, 59, 881–900.

Hollis, J.A., Harley, S.L., White, R.W., and Clarke, G.L. (2006) Preservation of evidence for prograde metamorphism in ultrahigh-temperature, high-pressure kyanite-bearing granulites, South Harris, Scotland. Journal of Metamorphic Geology, 24, 263–279.

Hollister, L.S. (1966) Garnet Zoning: An Interpretation Based on the Rayleigh Fractionation Model. Science, 154, 1647–1651.

Ikeda, T. (1993) Compositional zoning patterns of garnet during prograde metamorphism from the Yanai district, Ryoke metamorphic belt, southwest Japan. Lithos, 30, 109–121.

Karmakar, S. (2021) Formation of clinohumite ± spinel in dolomitic marbles from the Makrohar Granulite Belt, Central India: Evidence of Ti mobility during metamorphisim. American Mineralogist, 106, 1818–1827.

Karmakar, S., Bose, S., Sarbadhikari, A.B., and Das, K. (2011) Evolution of granulite enclaves and associated gneisses from Purulia, Chhotanagpur Granite Gneiss Complex, India: Evidence for 990-940Ma tectonothermal event(s) at the eastern India cratonic fringe zone. Journal of Asian Earth Sciences, 41, 69–88.

Karmakar, S., Mukherjee, S., Sanyal, S., and Sengupta, P. (2017) Origin of peraluminous minerals (corundum, spinel, and sapphirine) in a highly calcic anorthosite from the Sittampundi Layered Complex, Tamil Nadu, India. Contributions to Mineralogy and Petrology, 172, 67.

Kelsey, D.E., and Hand, M. (2015) On ultrahigh temperature crustal metamorphism: Phase equilibria, trace element thermometry, bulk composition, heat sources, timescales and tectonic settings. Geoscience Frontiers, 6, 311–356.

Kohn, M.J. (2014) Geochemical Zoning in Metamorphic Minerals. Treatise on Geochemistry: Second Edition, 4, 249–280.

Lanari, P., Vidal, O., De Andrade, V., Dubacq, B., Lewin, E., Grosch, E.G., and Schwartz, S. (2014) XMapTools: A MATLAB©-based program for electron microprobe X-ray image processing and geothermobarometry. Computers and Geosciences, 62, 227–240.

Lanari, P., Vho, A., Bovay, T., Airaghi, L., and Centrella, S. (2019) Quantitative compositional mapping of mineral phases by electron probe micro-analyser. Geological Society Special Publication, 478, 39–63.

Lang, H.M., and Rice, J.M. (1985) Regression modelling of metamorphic reactions in

metapelites, snow peak, Northern Idaho. Journal of Petrology, 26, 857–887.

Lang, H.M., Watcher, A.J., Peterson, V.L., and Ryan, J.G. (2004) Coexisting clinopyroxene/spinel and amphibole/spinel symplectites in metatroctolites from the Buck Creek ultramafic body, North Carolina Blue Ridge. American Mineralogist, 89, 20–30.

Lasaga, A.C. (1981) Atomistic basis of kinetics: defects in minerals. Reviews in Mineralogy & Geochemistry, 8, 261–316.

Leake, B.E., Woolley, A.R., Arps, C.E.S., Birch, W.D., Gilbert, M.C., Grice, J.D., Hawthorne, F.C., Kato, A., Kisch, H.J., Krivovichev, V.G., and others (1997) Nomenclature of amphiboles: Report of the subcommittee on amphiboles of the international mineralogical association, commission on new minerals and mineral names. Canadian Mineralogist, 35, 219–246.

Leake, B.E., Mogessie, A., and Ettinger, K. (2004) AMPH-IMA04: a revised Hypercard program to determine the name of an amphibole from chemical analyses according to the 2004 International Mineralogical Association scheme. Mineralogical Magazine, 68, 825–830.

Liou, J.G., Zhang, R., and Ernst, W.G. (1998) Mineral parageneses in the Piampaludo eclogitic body, Gruppo di Voltri, Western Ligurian Alps. Schweizerische mineralogische und petrographische Mitteilungen, 78, 317.

Litasov, K.D., Malkovets, V.G., Kostrovitsky, S.I., and Taylor, L.A. (2003) Petrogenesis of ilmenite-bearing symplectite xenoliths from vitim alkaline basalts and yakutian kimberlites, Russia. International Geology Review, 45, 976–997.

Liu, P., and Massonne, H.J. (2022) High-pressure granulite facies re-equilibration and zoisite–biotite dehydration melting during decompression of an ultrahigh-pressure garnet clinopyroxenite from the island of Fjørtoft, Norway. Journal of Metamorphic Geology, 40,

887–918.

Liu, T., Jiang, S.Y., Zheng, R.H., and Chen, W. (2022) Titanite U-Pb dating and geochemical constraints on the Paleozoic magmatic-metamorphic events and Nb-Ta mineralization in the Yushishan deposit, South Qilian, NW China. Lithos, 412–413, 106612.

Lopez Ruiz, J. (1976) The Zoning of Garnets As an Indicator of the P.T. history of their host-rocks. Annales de la Société Géologique de Belgique, 99, 337–346.

Lucassen, F., Franz, G., Rhede, D., and Wirth, R. (2010) Ti-Al zoning of experimentally grown titanite in the system CaO-Al 2O3-TiO2-SiO2- NaCl-H2O-(F): Evidence for small-scale fluid heterogeneity. American Mineralogist, 95, 1365–1378.

Marsh, J.H., and Kelly, E.D. (2017) Petrogenetic relations among titanium-rich minerals in an anatectic high-P mafic granulite. Journal of Metamorphic Geology, 35, 717–738.

Morimoto, N. (1988) Nomenclature of pyroxenes: subcommitee on pyroxenes Commission on New Minerals and Mineral Names (CNMMN) International Mineral Association (IMA). Schweizerische Mineralogische und Petrographische Mitteilungen, 68, 95–111.

Mukherjee, S., Dey, A., and Sanyal, S. (2017) Petrology and U – Pb geochronology of zircon in a suite of charnockitic gneisses from parts of the Chotanagpur Granite Gneiss Complex ( CGGC ): evidence for the reworking of a Mesoproterozoic basement during the formation of the Rodinia supercontinent. Geological Society, London, Special Publications, 457.

Mukherjee, S., Dey, A., Ibanez-mejia, M., Sanyal, S., and Sengupta, P. (2018a) Geochemistry , U-Pb geochronology and Lu-Hf isotope systematics of a suite of ferroan ( A-type ) granitoids from the CGGC : Evidence for Mesoproterozoic crustal extension in the east Indian shield. Precambrian Research, 305, 40–63.

Mukherjee, S., Dey, A., Sanyal, S., and Sengupta, P. (2018b) Tectonothermal imprints in a suite

of mafic dykes from the Chotanagpur Granite Gneissic complex (CGGC), Jharkhand, India: Evidence for late Tonian reworking of an early Tonian continental crust. Lithos, 320–321, 490–514.

——— (2019) Proterozoic crustal evolution of the Chotanagpur granite Gneissic Complex, Jharkhand-Bihar-West Bengal, India: Current status and future prospect. Springer Geology, 7–54.

Nixon, P.H., and Boyd, F.R. (1979) Garnet bearing lherzolites and discrete nodule suites from the Malaita Alnoite, Solomon Islands, S.W. Pacific, and their bearing on oceanic mantle composition and geotherm. The Mantle Sample: Inclusion in Kimberlites and Other Volcanics, 16, 400–423.

Nyström, A.I., and Kriegsman, L.M. (2003) Prograde and retrograde reactions, garnet zoning patterns, and accessory phase behaviour in SW Finland migmatites, with implications for geochronology. Geological Society Special Publication, 220, 213–230.

O'Brien, P.J., and Rötzler, J. (2003) High-pressure granulites: Formation, recovery of peak conditions and implications for tectonics. Journal of Metamorphic Geology, 21, 3–20.

Palin, R.M., Weller, O.M., Waters, D.J., and Dyck, B. (2016) Quantifying geological uncertainty in metamorphic phase equilibria modelling ; a Monte Carlo assessment and implications for tectonic interpretations. Geoscience Frontiers, 7, 591–607.

Pattison, D.R.M. (2003) Petrogenetic significance of orthopyroxene-free garnet + clinopyroxene + plagioclase ± quartz-bearing metabasites with respect to the amphibolite and granulite facies. Journal of Metamorphic Geology, 21, 21–34.

Purtov, V.K., and Kotel'nikova, A.L. (1993) Solubility of titanium in chloride and fluoride hydrothermal solutions. International Geology Review, 35, 279–287.

Putnis, A. (2002) Mineral replacement reactions: from macroscopic observations to microscopic mechanisms. Mineralogical Magazine, 66, 689–708.

Putnis, A. (2009) Mineral replacement reactions. Reviews in Mineralogy and Geochemistry, 70, 87–124.

Putnis, A., and Putnis, C. V. (2007) The mechanism of reequilibration of solids in the presence of a fluid phase. Journal of Solid State Chemistry, 180, 1783–1786.

Rapp, J.F., Klemme, S., Butler, I.B., and Harley, S.L. (2010) Extremely high solubility of rutile in chloride and fluoride-bearing metamorphic fluids: An experimental investigation. Geology, 38, 323–326.

Rekha, S., Upadhyay, D., Bhattacharya, A., Kooijman, E., Goon, S., Mahato, S., and Pant, N.C. (2011) Lithostructural and chronological constraints for tectonic restoration of Proterozoic accretion in the Eastern Indian Precambrian shield. Precambrian Research, 187, 313–333.

Remmert, P., Heinrich, W., Wunder, B., Morales, L., Wirth, R., Rhede, D., and Abart, R. (2018) Synthesis of monticellite–forsterite and merwinite–forsterite symplectites in the CaO–MgO–SiO2 model system: influence of temperature and water content on microstructure evolution. Contributions to Mineralogy and Petrology, 173, 1–17.

Ringwood, A.E., and Lovering, J.F. (1970) Significance of pyroxene-ilmenite intergrowth among kimberlite xenoliths. Earth and Planetary Science Letters, 7, 371–375.

Romer, R.L., and Rötzler, J. (2003, January 1) Effect of metamorphic reaction history on the U-Pb dating of titanite. (D. Vance, W. Müller, & I.M. Villa, Eds.)Geological Society, London, Special Publications. Geological Society of London.

Rötzler, J., and Romer, R.L. (2001) P-T-t evolution of ultrahigh-temperature granulites from the Saxon Granulite Massif, Germany. Part I: Petrology. Journal of Petrology, 42, 1995–2013.

Rötzler, J., Romer, R.L., Budzinski, H., and Oberhänsli, R. (2004) Ultrahigh-temperature high-pressure granulites from Tirschheim, Saxon Granulite Massif, Germany: P-T-t path and geotectonic implications. European Journal of Mineralogy, 16, 917–937.

Ruiz-Agudo, E., Putnis, C. V., and Putnis, A. (2014) Coupled dissolution and precipitation at mineral-fluid interfaces. Chemical Geology, 383, 132–146.

Ryzhenko, B.N., Kovalenko, N.I., and Prisyagina, N.I. (2006) Titanium complexation in hydrothermal systems. Geochemistry International, 44, 879–895.

Sanyal, S., and Sengupta, P. (2012) Metamorphic evolution of the Chotanagpur Granite Gneiss Complex of the East Indian Shield : current status. Geological Society, London, Special Publications, 365, 117–145.

Saxena, S., and Ganguly, J. (1987) Mixtures and mineral reactions.

Scibiorski, E., Kirkland, C.L., Kemp, A.I.S., Tohver, E., and Evans, N.J. (2019) Trace elements in titanite: A potential tool to constrain polygenetic growth processes and timing. Chemical Geology, 509, 1–19.

Sengupta, P., and Dasgupta, S. (2009) Modelling of Metamorphic Textures with C-Space: Evidence of Pan-African High-grade Reworking in the Eastern Ghats Belt, India. In Physics and Chemistry of the Earth's Interior pp. 29–39.

Sengupta, P., Raith, M.M., and Levitsky, V.I. (2004) Compositional characteristics and paragenetic relations of magnesiohögbomite in aluminous amphibolites from the Belomorian complex, Baltic Shield, Russia. American Mineralogist, 89, 819–831.

Sengupta, P., Dutta, U., Bhui, U.K., and Mukhopadhyay, D. (2009) Genesis of wollastonite- and grandite-rich skarns in a suite of marble-calc-silicate rocks from Sittampundi, Tamil Nadu: Constraints on the P-T-fluid regime in parts of the Pan-African mobile belt of South India.

Mineralogy and Petrology, 95, 179–200.

Spear, F.S. (1993) Metamorphic Phase Equilibria and Pressure-temperature-time Paths. Mineralogical Society of America.

Tanis, E.A., Simon, A., Zhang, Y., Chow, P., Xiao, Y., Hanchar, J.M., Tschauner, O., and Shen, G. (2016) Rutile solubility in NaF-NaCl-KCl-bearing aqueous fluids at 0.5-2.79 GPa and 250-650 °C. Geochimica et Cosmochimica Acta, 177, 170–181.

Timmerman, M. (2004) Timing, geodynamic setting and character of Permo-Carboniferous magmatism in the foreland of the Variscan Orogen, NW Europe. Geological Society, London, Special Publications, 223, 41–74.

Torres-Roldan, R.L., Garcia-Casco, A., and Garcia-Sanchez, P.A. (2000) CSpace: An integrated workplace for the graphical and algebraic analysis of phase assemblages on 32-bit wintel platforms. Computers and Geosciences, 26, 779–793.

Tropper, P., and Manning, C.E. (2005) Very low solubility of rutile in H2O at high pressure and temperature, and its implications for Ti mobility in subduction zones. American Mineralogist, 90, 502–505.

Tuccillo, M.E., Essene, E.J., and Van Der Pluijm, B.A. (1990) Growth and retrograde zoning in garnets from high-grade metapelites: implications for pressure-temperature paths. Geology, 18, 839–842.

Vielzeuf, D., and Schmidt, M.W. (2001) Melting relations in hydrous systems revisited: Application to metapelites, metagreywackes and metabasalts. Contributions to Mineralogy and Petrology, 141, 251–267.

Watkins, J.M., Clemens, J.D., and Treloar, P.J. (2007) Archaean TTGs as sources of younger granitic magmas: Melting of sodic metatonalites at 0.6-1.2 GPa. Contributions to

Mineralogy and Petrology, 154, 91–110.

Watson, E.B., and Baxter, E.F. (2007) Diffusion in solid-Earth systems. Earth and Planetary Science Letters, 253, 307–327.

Whitney, D.L., and Evans, B.W. (2010) Abbreviations for Names of Rock-Forming Minerals. American Mineralogist, 95, 185–187.

Xiao, X., Zhou, T., White, N.C., Zhang, L., Fan, Y., and Chen, X. (2021) Multiple generations of titanites and their geochemical characteristics record the magmatic-hydrothermal processes and timing of the Dongguashan porphyry-skarn Cu-Au system , Tongling district , Eastern China. Mineralium Deposita, 56, 363–380.

Zhang, R.Y., Zhai, S.M., Fei, Y.W., and Liou, J.G. (2003) Titanium solubility in coexisting garnet and clinopyroxene at very high pressure: The significance of exsolved rutile in garnet. Earth and Planetary Science Letters, 216, 591–601.

Zhou, K., Chen, Y., and Zheng, Y. (2021) Geochemistry of polygenetic titanite traces metamorphic and anatectic processes during the exhumation of deeply subducted continental crust. LITHOS, 398–399, 106314.

## FIGURE CAPTIONS

**Figure 1.(a)** Geological map representing different domains of CGGC (after Mukherjee et al. 2019). The boxed area represents the study area. **(b)** Lithological map of the study area showing Masanjore and the adjoining areas adapted and modified after the Geological and mineral map/

district resource map of Dumka district, Jharkhand (Geological Survey of India, year 2009), also showing the locations of the studied mafic granulites. **(c)** The studied mafic granulites showed a medium-grained massive appearance, comprising garnet, clinopyroxene, plagioclase, and amphibole. Garnet porphyroblasts (≤1cm diameter) are distributed uniformly in the rock. **(d)** Coarse-grained amoeboid patches or segregations comprising plagioclase, garnet, amphibole, quartz, and clinopyroxene. The coarse-grained patches are surrounded by amphibole, separating it from the medium-grained host rock.

**Figure 2.** Photomicrographs and BSE images showing textural relations:**(a)** Garnet porphyroblasts of variable size and, medium-grained clinopyroxene ($Cpx_1$) and plagioclase ($Pl_1$) are forming the granoblastic mosaic matrix. Secondary amphibole ($Amp_2$) is replacing both $Cpx_1$ and garnet. **(b)** Quartz present in the matrix is reacting with garnet porphyroblasts to form a double corona of clinopyroxene ($Cpx_2$) and plagioclase ($Pl_2$). **(c)** Secondary amphibole($Amp_2$) is replacing garnet porphyroblasts along its boundary, while primary amphibole ($Amp_0$) is present as inclusion within garnet. **(d)** Matrix clinopyroxene (Cpx1) hosts inclusions of plagioclase ($Pl_0$) and amphibole ($Amp_0$). **(e)** Garnet contains ilmenite inclusion that is successively rimmed by rutile and plagioclase. **(f)** Rutile is present in the rock matrix and also in contact with $Amp_2$. **(g)** Titanite appears to be stranded within $Amp_2$which is replacing $Cpx_1$. **(h)** Secondary amphibole ($Amp_2$) is replacing garnet porphyroblasts both along its boundary and fracture planes. **(i)** Amphibole ($Amp_2$) is replacing matrix clinopyroxene ($Cpx_1$) along its boundary and cleavage planes.

**Figure 3.**Photomicrographs and BSE images showing textural relations:**(a)** Titanite is present in the rock matrix in contact with $Cpx_1$ and is getting replaced by a symplectic intergrowth of Ilm and clinopyroxene ($Cpx_2$). **(b)** Titanite is almost completely replaced by the symplectic

intergrowth of Ilm and $Cpx_2$. **(c)** Clinopyroxene ($Cpx_2^{ILM}$)-ilmenite intergrowth is separated from porphyroblastic garnet by a rind of plagioclase ($Pl_2$). Small rounded grain of titanite (relict) is present within the plagioclase rind. **(d)**$Cpx_2^{ILM}$-Ilm symplectic intergrowth is set apart from porphyroblastic garnet by the symplectic intergrowth of clinopyroxene ($Cpx_2^{PL}$) and plagioclase ($Pl_2$). The $Cpx_2^{ILM}$-Ilm symplectite is extremely fine-grained (lamellar width <2μm) towards the inside of the symplectic intergrowth. Lamellar width of the symplectite increases towards the outer margin (~55 μm) of the intergrowth. **(e)**$Cpx_2^{ILM}$-Ilm symplectite with relict titanite is separated from garnet by the $Cpx_2^{PL}$-$Pl_2$ symplectite. These two symplectites are adjacent to each other but the $Cpx_2^{ILM}$-Ilm symplectite is proximal to titanite and the $Cpx_2^{PL}$-$Pl_2$ symplectite is proximal to garnet. Amphibole ($Amp_2$) is partially replacing clinopyroxene ($Cpx_2^{PL}$) in the symplectic intergrowth **(f)** Symplectic clinopyroxene ($Cpx_2^{ILM}$) in association with ilmenite is replaced by amphibole, such that amphibole appears to form symplectic intergrowths with ilmenite.

**Figure 4. (a-c)** X-ray intensity maps of Mn (a), Ca (b), and Fe (c) of a porphyroblastic garnet. All three maps show flat homogenous core composition extending up to the rim, which is thin. The X-ray intensity map of Mn shows a drastic increase in intensity in the thin rim, while the map of Fe shows a slight increase in intensity. The X-ray intensity map of Ca shows a dip in intensity in the rim.The area marked in the X-ray intensity map of Mn (a) is magnified in the X-ray intensity maps of figure d-h (same domainas Figure 3.d; Domain II). **(d-h)** These represent X-ray intensity maps of Mg, Fe, Mn, Ca, and Ti respectively. X-ray intensity elemental map of Mg (d) indicates restricted occurrences of orthopyroxene within this symplectic intergrowth of $Cpx_2^{ILM}$-Ilm. The X-ray intensity map of Mg (d) also shows a dip in intensity in the rim of garnet porphyroblasts. Very fine grains of apatite are present in the $Cpx_2^{ILM}$-Ilm symplectic intergrowth.

**(i)**Plots showing compositional variation (or similarity) in clinopyroxene and orthopyroxene (Morimoto 1988) occurring in different textural settings.

**Figure 5. (a-g)** Elemental X-ray intensity maps of Si, Al, Ti, Fe, Mg, Na, Ca from the same region of Fig. 3.c (Domain I). Fine-grained apatite is present within the $Cpx_2$-Ilm symplectites (red dots in the Ca map). **(h)** A Composite CaO map processed in the XMapTools software is used to calculate phase proportions of ilmenite and clinopyroxene in the $Cpx_2^{ILM}$-Ilm symplectites in the textural modeling study.

**Figure 6. (a)** P-T pseudosection corresponding to the EBC (obtained from Domain II (Fig. 3.d) by XMapTools) is calculated in the NCFMASHT ($Na_2O$-CaO-FeO-MgO-$Al_2O_3$-$SiO_2$-$H_2O$-$TiO_2$) system where amphibole, melt, plagioclase, garnet, sphene, ilmenite, clinopyroxene, orthopyroxene "IN" lines are marked. **(b)** Compositional isopleths for garnet ($X_{ALM}$, $X_{PRP}$, $X_{GRS}$) and plagioclase ($X_{AN}$) plotted on the pseudosection in the appropriate assemblage fields, constrain the P-T conditions of peak and retrogression. P-T conditions estimated using conventional thermobarometry are also plotted in the diagram with the "plus" signs with red (peak) and green (retrogression) squares. P-T conditions estimate a steeply positive P-T path (near isothermal). Dotted lines represent various possible prograde paths. **(c)** Volume isopleths of Grt, rutile and titanite are plotted on the pseudosection. **(d)** Change in volume proportion of the major phases (Grt, Cpx, Opx, melt, Pl ) and **(e)** Change in the volume proportions of the Ti-bearing phases (Ilm, Spn, Rt ) during a pressure drop of 13 to 7 kbar at 850°C, i.e. along the estimated P-T path, is shown.

**Figure 7. (a-b)** Textural modeling studies from Domain I-II suggest mobility of several chemical species across the initial boundary between garnet and titanite. In both domains, FeO and MgO are moving from the garnet end toward the titanite end. In both domains $P_2O_5$, $Na_2O$, F, and Cl

are coming from external sources. The direction of CaO movement is reversed between Domain-I and II. Domain II requires an external source of CaO while Domain I is releasing CaO outside.

Table 1: Representative microprobe analyses and calculated cations of garnet based on 12 oxygens

| Sample | SM128A1 | SM128A1 | SM128A1 | SM128A1 | SM128A1 | SM128A1 | SM128A1 | SM128A1 |
|---|---|---|---|---|---|---|---|---|
| Sr. no. | G-1 | G-2 | G-3 | G-4 | G-5 | G-6 | G-7 | G-8 |
| Texture | Core | Rim | Core | Rim | Core | Rim | Core | Rim |
| $SiO_2$ | 38.50 | 36.93 | 38.41 | 38.43 | 38.41 | 36.90 | 38.19 | 38.38 |
| $TiO_2$ | 0.21 | 0.11 | 0.18 | 0.02 | 0.18 | 0.03 | 0.16 | 0.10 |
| $Al_2O_3$ | 21.51 | 20.88 | 21.64 | 21.12 | 21.64 | 20.81 | 21.44 | 21.35 |
| $Cr_2O_3$ | 0.01 | 0.07 | bdl | 0.08 | bdl | 0.04 | 0.06 | 0.14 |
| $Fe_2O_3$* | 2.05 | 4.35 | 2.99 | 0.51 | 2.99 | 3.17 | 3.00 | 1.81 |
| FeO* | 20.33 | 23.49 | 20.28 | 26.07 | 20.28 | 24.08 | 19.76 | 23.81 |
| MgO | 5.70 | 4.13 | 5.84 | 4.73 | 5.84 | 4.18 | 5.99 | 4.18 |
| CaO | 0.82 | 9.06 | 0.59 | 7.67 | 11.36 | 8.26 | 0.74 | 10.11 |
| MnO | 11.33 | 1.67 | 11.36 | 1.50 | 0.59 | 1.80 | 11.29 | 1.55 |
| $Na_2O$ | 0.05 | 0.01 | 0.05 | 0.01 | 0.05 | 0.02 | 0.01 | -- |
| **Total** | 100.50 | 100.71 | 101.34 | 100.13 | 101.34 | 99.29 | 100.65 | 101.43 |
| Si | 2.96 | 2.90 | 2.93 | 3.01 | 2.93 | 2.93 | 2.93 | 2.97 |
| Ti | 0.01 | 0.01 | 0.01 | -- | 0.01 | -- | 0.01 | 0.01 |
| Al | 1.95 | 1.93 | 1.95 | 1.95 | 1.95 | 1.95 | 1.94 | 1.95 |
| Cr | -- | -- | -- | -- | -- | -- | -- | 0.01 |
| $Fe^{+3}$* | 0.12 | 0.26 | 0.17 | 0.03 | 0.17 | 0.19 | 0.17 | 0.11 |
| $Fe^{+2}$* | 1.31 | 1.54 | 1.30 | 1.71 | 1.30 | 1.60 | 1.27 | 1.54 |
| Mg | 0.65 | 0.48 | 0.67 | 0.55 | 0.67 | 0.50 | 0.69 | 0.48 |
| Ca | 0.93 | 0.76 | 0.93 | 0.64 | 0.93 | 0.70 | 0.93 | 0.84 |
| Mn | 0.05 | 0.11 | 0.04 | 0.10 | 0.04 | 0.12 | 0.05 | 0.10 |
| Na | 0.01 | -- | 0.01 | -- | 0.01 | -- | -- | -- |
| $X_{ALM}$ | 0.44 | 0.53 | 0.44 | 0.57 | 0.44 | 0.55 | 0.43 | 0.52 |
| $X_{GRS}$ | 0.32 | 0.26 | 0.32 | 0.21 | 0.32 | 0.24 | 0.32 | 0.28 |
| $X_{PRP}$ | 0.22 | 0.17 | 0.23 | 0.18 | 0.23 | 0.17 | 0.23 | 0.16 |
| $X_{SPSS}$ | 0.02 | 0.04 | 0.01 | 0.03 | 0.01 | 0.04 | 0.02 | 0.03 |
| $X_{Mg}$ | 0.33 | 0.24 | 0.34 | 0.24 | 0.34 | 0.24 | 0.35 | 0.24 |

*$Fe_2O_3$ and $Fe^{+3}$ is recalculated after the scheme of Droop (1987)

| SM128A5 | SM128A1 | SM128A1$^{DM2}$ | SM128A$^{DM1}$ |
|---|---|---|---|
| G-9 | G-10 | G-11 | G-12 |
| Core | Rim | Core | Core |
| 39.37 | 39.00 | 38.50 | 39.28 |
| 0.18 | 0.03 | 0.21 | 0.24 |
| 21.55 | 21.94 | 21.51 | 21.72 |
| 0.04 | 0.10 | 0.01 | bdl |
| 0.26 | 0.17 | 2.05 | 0.99 |
| 21.23 | 25.69 | 20.33 | 22.09 |
| 5.47 | 5.12 | 5.70 | 5.61 |
| 12.09 | 7.97 | 11.33 | 10.71 |
| 0.83 | 1.48 | 0.82 | 0.88 |
| 0.01 | 0.02 | 0.05 | 0.06 |
| 101.03 | 101.52 | 100.50 | 101.57 |
| 3.01 | 3.00 | 2.96 | 2.99 |
| 0.01 | -- | 0.01 | 0.01 |
| 1.94 | 1.99 | 1.95 | 1.95 |
| -- | 0.01 | -- | -- |
| 0.01 | 0.01 | 0.12 | 0.06 |
| 1.36 | 1.65 | 1.31 | 1.41 |
| 0.62 | 0.59 | 0.65 | 0.64 |
| 0.99 | 0.66 | 0.93 | 0.87 |
| 0.05 | 0.10 | 0.05 | 0.06 |
| -- | -- | 0.01 | 0.01 |
| 0.45 | 0.55 | 0.44 | 0.47 |
| 0.33 | 0.22 | 0.32 | 0.29 |
| 0.21 | 0.20 | 0.22 | 0.21 |
| 0.02 | 0.03 | 0.02 | 0.02 |
| 0.31 | 0.26 | 0.33 | 0.31 |

Table 2: Representative microprobe analyses and calculated cations of pyroxene based on 6 oxygens

| Sample | SM128A1 | SM128A1 | SM128A1 | SM128A1 | SM128A1 | SM128A1 | SM128A1 | SM128A1 | SM128A5 |
|---|---|---|---|---|---|---|---|---|---|
| Sr. No. | Px-1 | Px-2 | Px-3 | Px-4 | Px-5 | Px-6 | Px-7 | Px-8 | Px-9 |
| Texture | Cpx1 | $Cpx_2^{PL}$ | Cpx1 | $Cpx_2^{PL}$ | Cpx1 | $Cpx_2^{PL}$ | Cpx1 | $Cpx_2^{PL}$ | Cpx1 |
| $SiO_2$ | 50.32 | 51.61 | 51.00 | 52.43 | 48.68 | 52.25 | 51.15 | 52.00 | 50.67 |
| $TiO_2$ | 0.56 | 0.13 | 0.40 | 0.19 | 0.63 | 0.12 | 0.34 | 0.25 | 0.54 |
| $Al_2O_3$ | 4.41 | 1.44 | 3.94 | 1.89 | 5.44 | 1.33 | 3.33 | 1.65 | 3.91 |
| $Cr_2O_3$ | 0.06 | 0.23 | 0.00 | 0.36 | 0.06 | 0.36 | 0.11 | 0.00 | 0.00 |
| $Fe_2O_3$* | 4.11 | 1.62 | 2.99 | 0.00 | 4.58 | 1.86 | 2.39 | 2.01 | 2.60 |
| FeO* | 7.15 | 7.31 | 7.31 | 9.68 | 6.71 | 7.78 | 7.16 | 8.09 | 7.89 |
| MgO | 13.49 | 13.15 | 12.82 | 12.96 | 12.48 | 13.36 | 13.04 | 13.26 | 12.30 |
| CaO | 20.20 | 22.93 | 22.27 | 22.07 | 20.71 | 22.97 | 22.63 | 22.66 | 22.42 |
| MnO | 0.07 | 0.12 | 0.27 | 0.21 | 0.17 | 0.24 | 0.26 | 0.11 | 0.29 |
| $Na_2O$ | 0.72 | 0.34 | 0.54 | 0.30 | 0.70 | 0.29 | 0.41 | 0.31 | 0.50 |
| **Total** | 101.10 | 98.88 | 101.54 | 100.10 | 100.15 | 100.55 | 100.82 | 100.35 | 101.13 |
| Si | 1.86 | 1.95 | 1.88 | 1.96 | 1.82 | 1.95 | 1.89 | 1.94 | 1.88 |
| Ti | 0.02 | 0.00 | 0.01 | 0.01 | 0.02 | 0.00 | 0.01 | 0.01 | 0.02 |
| Al | 0.19 | 0.06 | 0.17 | 0.08 | 0.24 | 0.06 | 0.15 | 0.07 | 0.17 |
| Cr | 0.00 | 0.01 | 0.00 | 0.01 | 0.00 | 0.01 | 0.00 | 0.00 | 0.00 |
| $Fe^{+3}$* | 0.11 | 0.05 | 0.08 | 0.00 | 0.13 | 0.05 | 0.07 | 0.06 | 0.07 |
| $Fe^{+2}$* | 0.22 | 0.23 | 0.22 | 0.30 | 0.21 | 0.24 | 0.22 | 0.25 | 0.24 |
| Mg | 0.74 | 0.74 | 0.70 | 0.72 | 0.69 | 0.74 | 0.72 | 0.74 | 0.68 |
| Ca | 0.80 | 0.93 | 0.88 | 0.88 | 0.83 | 0.92 | 0.90 | 0.91 | 0.89 |
| Mn | 0.00 | 0.00 | 0.01 | 0.01 | 0.01 | 0.01 | 0.01 | 0.00 | 0.01 |
| Na | 0.05 | 0.02 | 0.04 | 0.02 | 0.05 | 0.02 | 0.03 | 0.02 | 0.04 |
| $X_{Mg}$ | 0.77 | 0.76 | 0.76 | 0.70 | 0.77 | 0.75 | 0.76 | 0.74 | 0.74 |

*$Fe_2O_3$ and $Fe^{+3}$ is recalculated after the scheme of Droop (1987)

| SM128A1 | SM128A1$^{DM2}$ | SM128A1 | SM128A | SM128A$^{DM1}$ | SM128A1 | SM128A1 |
|---|---|---|---|---|---|---|
| Px-10 | Px-11 | Px-12 | Px-13 | Px-14 | Px-15 | Px-16 |
| $Cpx_2^{PL}$ | $Cpx_2^{ILM}$ | $Cpx_2^{ILM}$ | $Cpx_2^{ILM}$ | $Cpx_2^{ILM}$ | Opx | Opx |
| 53.04 | 53.00 | 51.53 | 52.33 | 53.33 | 52.05 | 51.45 |
| 0.14 | 0.38 | 0.46 | 0.22 | 0.32 | 0.58 | 0.08 |
| 1.29 | 1.16 | 1.12 | 1.45 | 1.05 | 0.78 | 0.89 |
| 0.00 | 0.09 | 0.07 | 0.00 | 0.00 | 0.02 | 0.03 |
| 0.07 | 1.15 | 2.22 | 2.17 | 0.41 | 0.93 | 3.47 |
| 9.56 | 8.66 | 7.17 | 8.75 | 10.43 | 25.53 | 26.95 |
| 13.23 | 13.65 | 13.49 | 13.04 | 12.79 | 20.21 | 18.54 |
| 22.38 | 23.01 | 22.89 | 22.67 | 22.85 | 0.42 | 0.54 |
| 0.23 | 0.18 | 0.23 | 0.13 | 0.04 | 0.49 | 0.51 |
| 0.31 | 0.23 | 0.26 | 0.33 | 0.31 | 0.03 | 0.01 |
| 100.24 | 101.50 | 99.43 | 101.08 | 101.52 | 101.04 | 102.46 |
| 1.98 | 1.96 | 1.94 | 1.94 | 1.97 | 1.95 | 1.93 |
| 0.00 | 0.01 | 0.01 | 0.01 | 0.01 | 0.02 | 0.00 |
| 0.06 | 0.05 | 0.05 | 0.06 | 0.05 | 0.03 | 0.04 |
| 0.00 | 0.00 | 0.00 | 0.00 | 0.00 | 0.00 | 0.00 |
| 0.00 | 0.03 | 0.06 | 0.06 | 0.01 | 0.03 | 0.10 |
| 0.30 | 0.27 | 0.23 | 0.27 | 0.32 | 0.80 | 0.85 |
| 0.74 | 0.75 | 0.76 | 0.72 | 0.71 | 1.13 | 1.04 |
| 0.89 | 0.91 | 0.92 | 0.90 | 0.91 | 0.02 | 0.02 |
| 0.01 | 0.01 | 0.01 | 0.00 | 0.00 | 0.02 | 0.02 |
| 0.02 | 0.02 | 0.02 | 0.02 | 0.02 | 0.00 | 0.00 |
| 0.71 | 0.74 | 0.77 | 0.73 | 0.69 | 0.59 | 0.55 |

Table 3: Representative microprobe analyses and calculated cations of plagioclase based on 8 oxygens

| Sample | SM128A1 | SM128A1 | SM128A1 | SM128A1 | SM128A1 | SM128A1 | SM128A1 | SM128A1$^{DMII}$ | SM128A5 |
|---|---|---|---|---|---|---|---|---|---|
| Sr. no. | Pl-1 | Pl-2 | Pl-3 | Pl-4 | Pl-5 | Pl-6 | Pl-7 | Pl-8 | Pl-9 |
| Texture | $Pl_1$ | $Pl_1$ | $Pl_1$ | $Pl_1$ | $Pl_1$ | $Pl_2$ | $Pl_1$ | $Pl_2$ | $Pl_1$ |
| | Core | Rim | Core | Rim | Core | Sym | Core | Sym | Core |
| $SiO_2$ | 56.96 | 47.66 | 56.74 | 47.28 | 57.07 | 47.43 | 56.41 | 48.05 | 57.90 |
| $Al_2O_3$ | 27.78 | 33.32 | 27.31 | 34.32 | 26.98 | 33.16 | 27.80 | 33.59 | 27.54 |
| FeO | 0.07 | 0.14 | 0.00 | 0.53 | 0.07 | 0.57 | 0.00 | 0.18 | 0.00 |
| MgO | 0.01 | 0.00 | 0.00 | 0.00 | 0.00 | 0.22 | 0.00 | 0.00 | 0.01 |
| CaO | 10.02 | 17.05 | 9.88 | 17.75 | 9.48 | 16.78 | 10.24 | 17.05 | 9.71 |
| $Na_2O$ | 6.41 | 1.90 | 6.51 | 1.57 | 6.77 | 1.63 | 6.27 | 1.90 | 6.46 |
| $K_2O$ | 0.05 | 0.01 | 0.07 | 0.02 | 0.10 | 0.09 | 0.04 | 0.01 | 0.10 |
| Total | 101.44 | 100.14 | 100.67 | 101.48 | 100.64 | 99.90 | 100.89 | 100.95 | 101.87 |
| Si | 2.53 | 2.18 | 2.54 | 2.15 | 2.55 | 2.18 | 2.52 | 2.19 | 2.55 |
| Al | 1.45 | 1.80 | 1.44 | 1.84 | 1.42 | 1.80 | 1.46 | 1.80 | 1.43 |
| $Fe^{+2}$ | 0.00 | 0.01 | 0.00 | 0.02 | 0.00 | 0.02 | 0.00 | 0.01 | 0.00 |
| Mg | 0.00 | 0.00 | 0.00 | 0.00 | 0.00 | 0.02 | 0.00 | 0.00 | 0.00 |
| Ca | 0.48 | 0.84 | 0.47 | 0.86 | 0.45 | 0.83 | 0.49 | 0.83 | 0.46 |
| Na | 0.55 | 0.17 | 0.56 | 0.14 | 0.59 | 0.15 | 0.54 | 0.17 | 0.55 |
| K | 0.00 | 0.00 | 0.00 | 0.00 | 0.01 | 0.01 | 0.00 | 0.00 | 0.01 |
| XOr | 0.00 | 0.00 | 0.00 | 0.00 | 0.01 | 0.01 | 0.00 | 0.00 | 0.01 |
| XAb | 0.54 | 0.17 | 0.54 | 0.14 | 0.56 | 0.15 | 0.52 | 0.17 | 0.54 |
| XAn | 0.46 | 0.83 | 0.45 | 0.86 | 0.43 | 0.85 | 0.47 | 0.83 | 0.45 |

| SM128A1 | SM128A[DMI] |
|---|---|
| Pl-10 | Pl-13 |
| $Pl_2$ | $Pl_2$ |
| Sym | rind |
| 47.78 | 50.81 |
| 33.56 | 31.87 |
| 0.10 | 0.35 |
| 0.00 | 0.01 |
| 16.94 | 14.79 |
| 1.92 | 3.42 |
| 0.01 | 0.02 |
| 100.41 | 101.32 |
| 2.18 | 2.29 |
| 1.81 | 1.69 |
| 0.00 | 0.01 |
| 0.00 | 0.00 |
| 0.83 | 0.71 |
| 0.17 | 0.30 |
| 0.00 | 0.00 |
| 0.00 | 0.00 |
| 0.17 | 0.29 |
| 0.83 | 0.70 |

Table 4: Representative microprobe analyses and calculated cations of amphibole based on 23 oxygens

| Sample | SM128A1 | SM128A1 | SM128A1 | SM128A | SM128A | SM128A | SM128A1 |
|---|---|---|---|---|---|---|---|
| Sr. no. | Am-1 | Am-2 | Am-3 | Am-4 | Am-5 | Am-6 | Am-7 |
| Phase | $Amp_2$ | $Amp_2$ | $Amp_2$ | $Amp_2$ | $Amp_2$ | $Amp_2$ | $Amp_0$ |
| $SiO_2$ | 45.11 | 46.02 | 45.78 | 45.28 | 45.26 | 46.03 | 44.76 |
| $TiO_2$ | 1.53 | 1.31 | 1.41 | 1.59 | 1.54 | 1.69 | 1.32 |
| $Al_2O_3$ | 11.09 | 10.65 | 10.26 | 10.65 | 10.65 | 9.88 | 11.96 |
| $Cr_2O_3$ | 0.31 | 0.23 | 0.17 | 0.01 | 0.07 | 0.04 | 0.00 |
| FeO | 15.14 | 13.90 | 14.68 | 15.90 | 16.30 | 16.34 | 14.66 |
| MgO | 11.55 | 12.64 | 12.10 | 11.76 | 11.86 | 11.28 | 12.75 |
| CaO | 11.47 | 11.65 | 11.41 | 11.32 | 11.49 | 11.38 | 11.84 |
| MnO | 0.17 | 0.00 | 0.14 | 0.16 | 0.13 | 0.17 | 0.09 |
| $Na_2O$ | 1.82 | 1.66 | 1.61 | 1.82 | 1.78 | 1.61 | 2.02 |
| $K_2O$ | 0.27 | 0.26 | 0.28 | 0.27 | 0.25 | 0.25 | 0.20 |
| F | 0.00 | 0.00 | 0.01 | 0.00 | 0.01 | 0.01 | 0.00 |
| Cl | 0.03 | 0.02 | 0.00 | 0.01 | 0.01 | 0.01 | 0.01 |
| Total | 98.49 | 98.33 | 97.83 | 98.78 | 99.34 | 98.68 | 99.68 |
| Si | 6.58 | 6.67 | 6.69 | 6.59 | 6.56 | 6.72 | 6.42 |
| $Al^{(IV)}$ | 1.42 | 1.33 | 1.31 | 1.41 | 1.44 | 1.28 | 1.58 |
| Ti | 0.00 | 0.00 | 0.00 | 0.00 | 0.00 | 0.00 | 0.00 |
| Sum T | 8.00 | 8.00 | 8.00 | 8.00 | 8.00 | 8.00 | 8.00 |
| $Al^{(VI)}$ | 0.49 | 0.49 | 0.46 | 0.42 | 0.38 | 0.42 | 0.45 |
| Ti | 0.17 | 0.14 | 0.15 | 0.17 | 0.17 | 0.19 | 0.14 |
| $Cr^{+3}$ | 0.04 | 0.03 | 0.02 | 0.00 | 0.01 | 0.00 | 0.00 |
| $Fe^{+3}$ | 0.26 | 0.25 | 0.28 | 0.35 | 0.41 | 0.27 | 0.44 |
| Mg | 2.51 | 2.73 | 2.63 | 2.55 | 2.56 | 2.45 | 2.73 |
| $Fe^{+2}$ | 1.54 | 1.36 | 1.45 | 1.51 | 1.48 | 1.67 | 1.25 |
| Mn | 0.00 | 0.00 | 0.00 | 0.00 | 0.00 | 0.00 | 0.00 |
| Sum C | 5.00 | 5.00 | 5.00 | 5.00 | 5.00 | 5.00 | 5.00 |
| Mg | 0.00 | 0.00 | 0.00 | 0.00 | 0.00 | 0.00 | 0.00 |
| $Fe^{+2}$ | 0.05 | 0.07 | 0.06 | 0.08 | 0.09 | 0.06 | 0.07 |
| Mn | 0.02 | 0.00 | 0.02 | 0.02 | 0.02 | 0.02 | 0.01 |
| Ca | 1.79 | 1.81 | 1.79 | 1.77 | 1.78 | 1.78 | 1.82 |
| Na | 0.13 | 0.12 | 0.13 | 0.14 | 0.12 | 0.14 | 0.10 |
| Sum B | 2.00 | 2.00 | 2.00 | 2.00 | 2.00 | 2.00 | 2.00 |
| Ca | 0.00 | 0.00 | 0.00 | 0.00 | 0.00 | 0.00 | 0.00 |
| Na | 0.38 | 0.35 | 0.32 | 0.38 | 0.38 | 0.31 | 0.47 |
| K | 0.05 | 0.05 | 0.05 | 0.05 | 0.05 | 0.05 | 0.04 |
| Sum A | 0.43 | 0.40 | 0.37 | 0.43 | 0.43 | 0.36 | 0.50 |
| TOTAL | 15.43 | 15.40 | 15.37 | 15.43 | 15.43 | 15.36 | 15.50 |
| $X_{Mg}$ | 0.61 | 0.66 | 0.64 | 0.62 | 0.62 | 0.59 | 0.67 |
| Group | Calcic group | Calcic group | Calcic group | Calcic group | Calcic group | Calcic group | Calcic group |
| Sub-Group | Magnesio-hornblend | Magnesio-hornblend | Magnesio-hornblend | Magnesio-hornblend | Magnesio-hornblend | Magnesio-hornblend | Pargasite |

| SM128A1 |
|---|
| Am-8 |
| $Amp_0$ |
| 43.83 |
| 1.56 |
| 11.92 |
| 0.30 |
| 15.34 |
| 11.85 |
| 11.65 |
| 0.02 |
| 1.99 |
| 0.29 |
| 0.00 |
| 0.02 |
| 98.86 |
| 6.39 |
| 1.61 |
| 0.00 |
| 8.00 |
| 0.43 |
| 0.17 |
| 0.03 |
| 0.38 |
| 2.57 |
| 1.41 |
| 0.00 |
| 5.00 |
| 0.00 |
| 0.08 |
| 0.00 |
| 1.82 |
| 0.10 |
| 2.00 |
| 0.00 |
| 0.47 |
| 0.05 |
| 0.52 |
| 15.52 |
| 0.63 |
| Calcic group |
| Pargasite |

Table 5: Representative microprobe analyses and calculated cations of Ti bearing phases and apatite

| Sample | SM128A1$^{DM2}$ | SM128A$^{DM1}$ | SM128A1$^{DM2}$ | SM128A1 | SM128A1 | SM128A$^{DM1}$ | SM128A | SM128A |
|---|---|---|---|---|---|---|---|---|
| Sr. no. | Tn-1 | Tn-2 | Im-1 | Im-2 | Im-3 | Im-4 | Im-5 | Im-6 |
| Phase | Ttn | Ttn | Ilm | Ilm | Ilm | Ilm | Ilm | Ilm |
| $SiO_2$ | 29.84 | 30.35 | 0.05 | 0.000 | 0.00 | 0.04 | 0.02 | 0.02 |
| $TiO_2$ | 38.67 | 39.35 | 51.03 | 52.134 | 52.39 | 51.18 | 51.63 | 51.81 |
| $Al_2O_3$ | 1.41 | 1.09 | 0.16 | 0.165 | 0.19 | 0.15 | 0.13 | 0.19 |
| $Cr_2O_3$ | 0.01 | 0.00 | 0.21 | 0.038 | 0.00 | 0.03 | 0.00 | 0.04 |
| $Fe_2O_3$* | 0.52 | 0.45 | 3.10 | 3.090 | 1.38 | 2.00 | 2.60 | 2.22 |
| FeO* | 0.00 | 0.00 | 42.74 | 44.063 | 42.67 | 43.53 | 44.49 | 44.79 |
| MgO | 0.04 | 0.00 | 1.20 | 1.134 | 1.57 | 0.74 | 0.72 | 0.62 |
| CaO | 28.98 | 28.64 | 0.11 | 0.050 | 0.17 | 0.20 | 0.17 | 0.10 |
| MnO | 0.09 | 0.05 | 0.53 | 0.569 | 0.49 | 0.42 | 0.38 | 0.58 |
| $Na_2O$ | 0.02 | 0.01 | 0.00 | 0.000 | 0.02 | 0.02 | 0.02 | 0.00 |
| F | 0.06 | 0.00 | 0.03 | 0.011 | 0.00 | 0.04 | 0.00 | 0.00 |
| $P_2O_5$ | 0.56 | 0.00 | 0.00 | 0.000 | 0.01 | 0.00 | 0.00 | 0.00 |
| Total | 100.20 | 99.94 | 99.16 | 101.25 | 98.88 | 98.36 | 100.15 | 100.36 |
| Oxygen | 5.00 | 5.00 | 3.00 | 3.000 | 3.00 | 3.00 | 3.00 | 3.00 |
| Si | 0.96 | 0.99 | 0.00 | 0.000 | 0.00 | 0.00 | 0.00 | 0.00 |
| Ti | 0.94 | 0.96 | 0.97 | 0.970 | 0.99 | 0.98 | 0.97 | 0.98 |
| Al | 0.05 | 0.04 | 0.00 | 0.005 | 0.01 | 0.00 | 0.00 | 0.01 |
| Cr | 0.00 | 0.00 | 0.00 | 0.001 | 0.00 | 0.00 | 0.00 | 0.00 |
| $Fe^{+3}$* | 0.01 | 0.01 | 0.06 | 0.058 | 0.03 | 0.04 | 0.05 | 0.04 |
| $Fe^{+2}$* | 0.00 | 0.00 | 0.90 | 0.911 | 0.89 | 0.93 | 0.93 | 0.94 |
| Mg | 0.00 | 0.00 | 0.05 | 0.042 | 0.06 | 0.03 | 0.03 | 0.02 |
| Ca | 1.00 | 1.00 | 0.00 | 0.001 | 0.00 | 0.01 | 0.00 | 0.00 |
| Mn | 0.00 | 0.00 | 0.01 | 0.012 | 0.01 | 0.01 | 0.01 | 0.01 |
| Na | 0.00 | 0.00 | 0.00 | 0.000 | 0.00 | 0.00 | 0.00 | 0.00 |
| F | 0.01 | 0.00 | 0.00 | 0.001 | 0.00 | 0.00 | 0.00 | 0.00 |
| P | 0.02 | 0.00 | 0.00 | 0.000 | 0.00 | 0.00 | 0.00 | 0.00 |

*$Fe_2O_3$ and $Fe^{+3}$ is recalculated after the scheme of Droop (1987)

| SM128B2 |
|---|
| Rt-1 |
| Rt |
| 0.00 |
| 98.14 |
| 0.35 |
| 0.03 |
| 0.86 |
| 0.00 |
| 0.02 |
| 0.02 |
| 0.00 |
| 0.00 |
| 0.04 |
| 0.00 |
| 99.46 |
| 2.00 |
| 0.00 |
| 0.97 |
| 0.01 |
| 0.00 |
| 0.01 |
| 0.00 |
| 0.00 |
| 0.00 |
| 0.00 |
| 0.00 |
| 0.00 |
| 0.00 |

| Sample | SM128A1 |
|---|---|
| Point | 10 |
| Phase | Ap |
| SiO2 | 0.033 |
| TiO2 | 0.024 |
| Al2O3 | 0 |
| Cr2O3 | 0 |
| FeO | 0.278 |
| MgO | 0.026 |
| CaO | 56.038 |
| MnO | 0.048 |
| Na2O | 0.05 |
| K2O | 0 |
| P2O5 | 42.155 |
| F | 1.657 |
| Cl | 0.24 |
| Sum | 100.55 |
| O=F | 0.70 |
| O=Cl | 0.05 |
| Revised SUM | 99.80 |
| Si | 0.00 |
| Ti | 0.00 |
| Al | 0.00 |
| Cr | 0.00 |
| Ca | 4.72 |
| Fe+2 | 0.02 |
| Mn | 0.00 |
| Mg | 0.00 |
| Na | 0.01 |
| K | 0.00 |
| P | 2.81 |
| SUM | 7.57 |
| F | 0.41 |
| Cl | 0.03 |
| OH | 0.56 |

Table 6: P-T estimates through conventional thermobarometric calculations

| Minerals in equilibrium | Dataset | | Thermometry (GC[1]) | |
|---|---|---|---|---|
| | No. | Phases used | P (ref) | T |
| ***Rt + Spn + Grt $_c$ + Cpx $_1$ + Pl $_1$*** | ***1*** | ***G-1; Px-1; Pl-1;*** | **13kbar** | 865°C |
| | ***2*** | ***G-3; Px-3; Pl-3;*** | | 825°C |
| | ***3*** | ***G-5; Px-5; Pl-5;*** | | 830°C |
| | ***4*** | ***G-7; Px-7; Pl-7;*** | | 844°C |
| | ***5*** | ***G-9; Px-9; Pl-9;*** | | 857°C |
| ***Ilm + Cpx $_2$ + Grt $_r$ + Opx + Pl $_2$*** | ***6*** | ***G-2; Px-2; Pl-2;*** | **7kbar** | 654°C |
| | ***7*** | ***G-4; Px-4; Pl-4;*** | | 693°C |
| | ***8*** | ***G-6; Px-6; Pl-6;*** | | 645°C |
| | **9** | ***G-8; Px-8; Pl-8;*** | | 690°C |
| | **10** | ***G-10; Px-10; Pl-10;*** | | 713°C |

[1]GC: Garnet – clinopyroxene geothermometer (Ellis and Green 1979).

[2]GCPS: Garnet – clinopyroxene – plagioclase – quartz barometer (Eckert et al. 1991).

| Barometry (GCPS$^2$) | |
|---|---|
| T (ref) | P |
| **850°C** | 12.6kbar |
| | 12.7kbar |
| | 13.0kbar |
| | 13.1kbar |
| | 12.6kbar |
| **700°C** | 7.4kbar |
| | 6.4kbar |
| | 6.8kbar |
| | 7.9kbar |
| | 6.8kbar |

# Figure 1

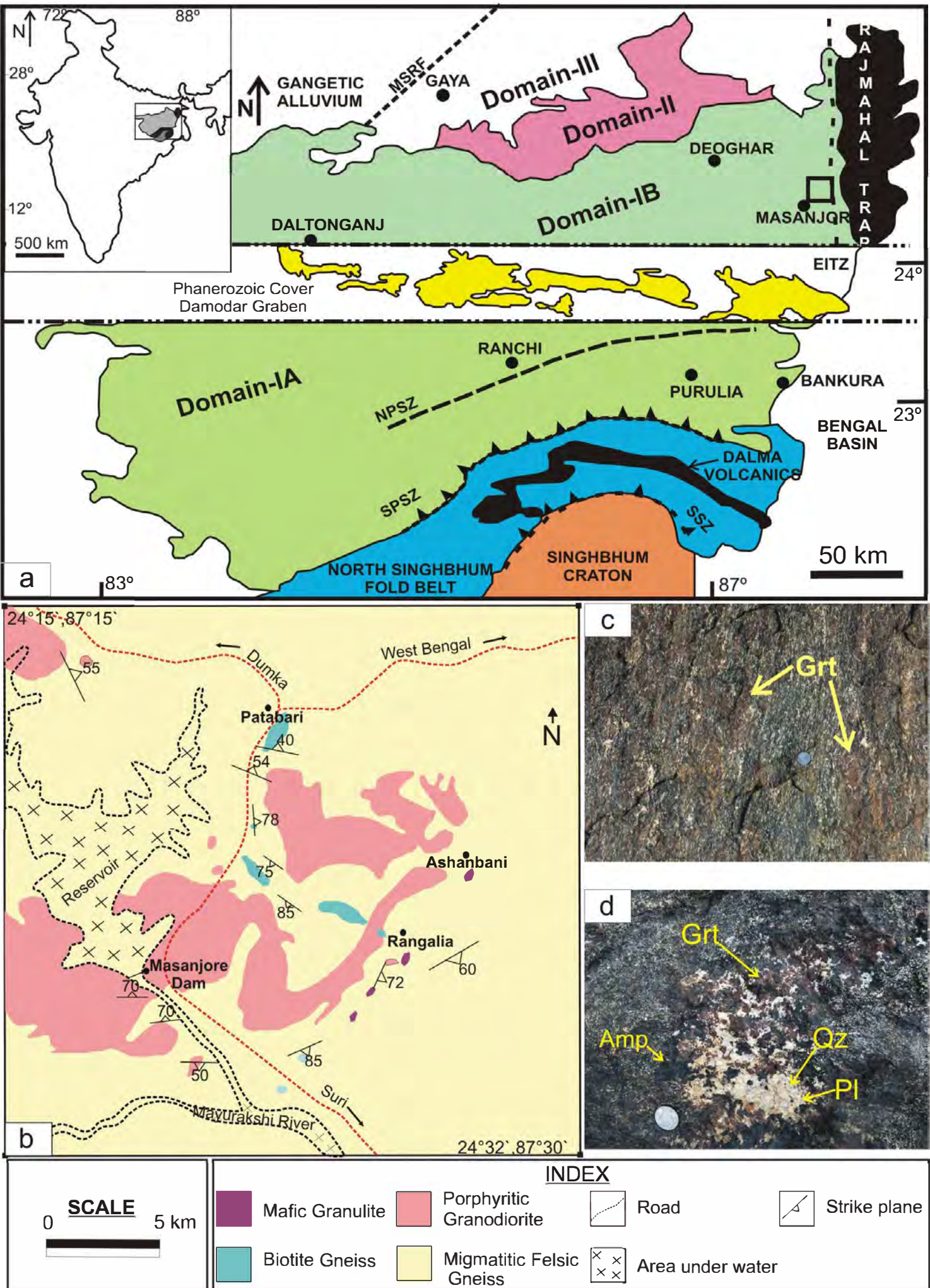
N
72°
88°
28°
12°
500 km
GANGETIC ALLUVIUM
MSRF
GAYA
Domain-III
Domain-II
DEOGHAR
RAJMAHAL TRAP
Domain-IB
DALTONGANJ
MASANJOR
EITZ
24°
Phanerozoic Cover
Damodar Graben
RANCHI
Domain-IA
NPSZ
PURULIA
BANKURA
23°
BENGAL BASIN
DALMA VOLCANICS
SPSZ
SSZ
SINGHBHUM CRATON
NORTH SINGHBHUM FOLD BELT
50 km
a
83°
87°
24°15`,87°15`
West Bengal
Dumka
Patabari
Ashanbani
Rangalia
Masanjore Dam
Reservoir
Suri
Mayurakshi River
24°32`,87°30`
b
c
Grt
d
Grt
Amp
Qz
Pl
SCALE
0
5 km
INDEX
Mafic Granulite
Porphyritic Granodiorite
Road
Strike plane
Biotite Gneiss
Migmatitic Felsic Gneiss
Area under water

Figure 2

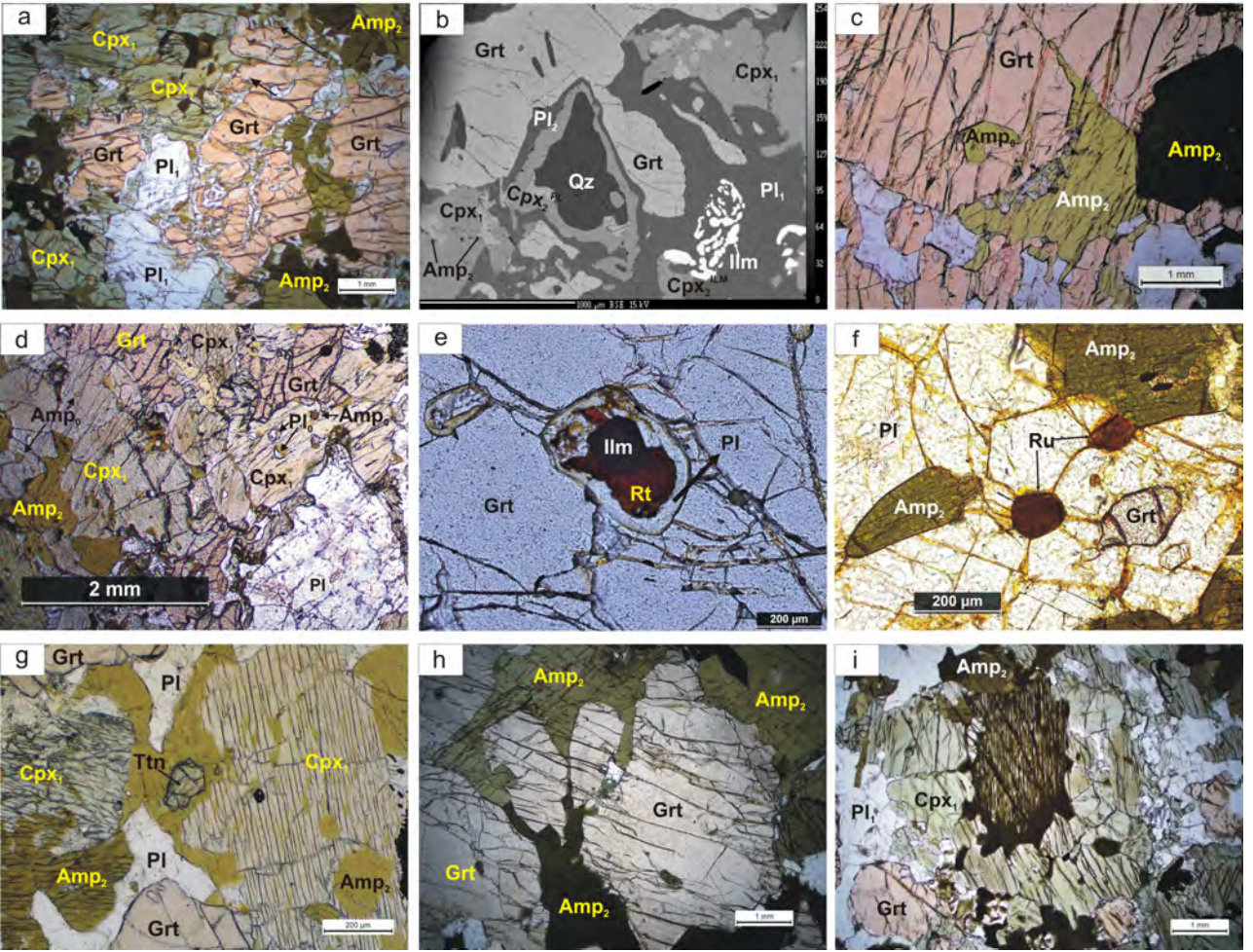
a
Cpx1
Amp2
Cpx1
Grt
Grt
Grt
Pl1
Cpx1
Pl1
Amp2
1 mm
b
Grt
Cpx1
Pl2
Grt
Qz
Pl1
Cpx1
Cpx2
Amp2
Ilm
Cpx2
c
Grt
Amp0
Amp2
Amp2
1 mm
d
Grt
Cpx1
Grt
Amp0
Pl0
Amp0
Cpx1
Cpx1
Amp2
2 mm
Pl
e
Ilm
Pl
Rt
Grt
200 µm
f
Amp2
Pl
Ru
Amp2
Grt
200 µm
g
Grt
Pl
Cpx1
Ttn
Cpx1
Amp2
Pl
Amp2
Grt
200 µm
h
Amp2
Amp2
Grt
Grt
Amp2
1 mm
i
Amp2
Pl1
Cpx1
Grt
1 mm

# Figure 3

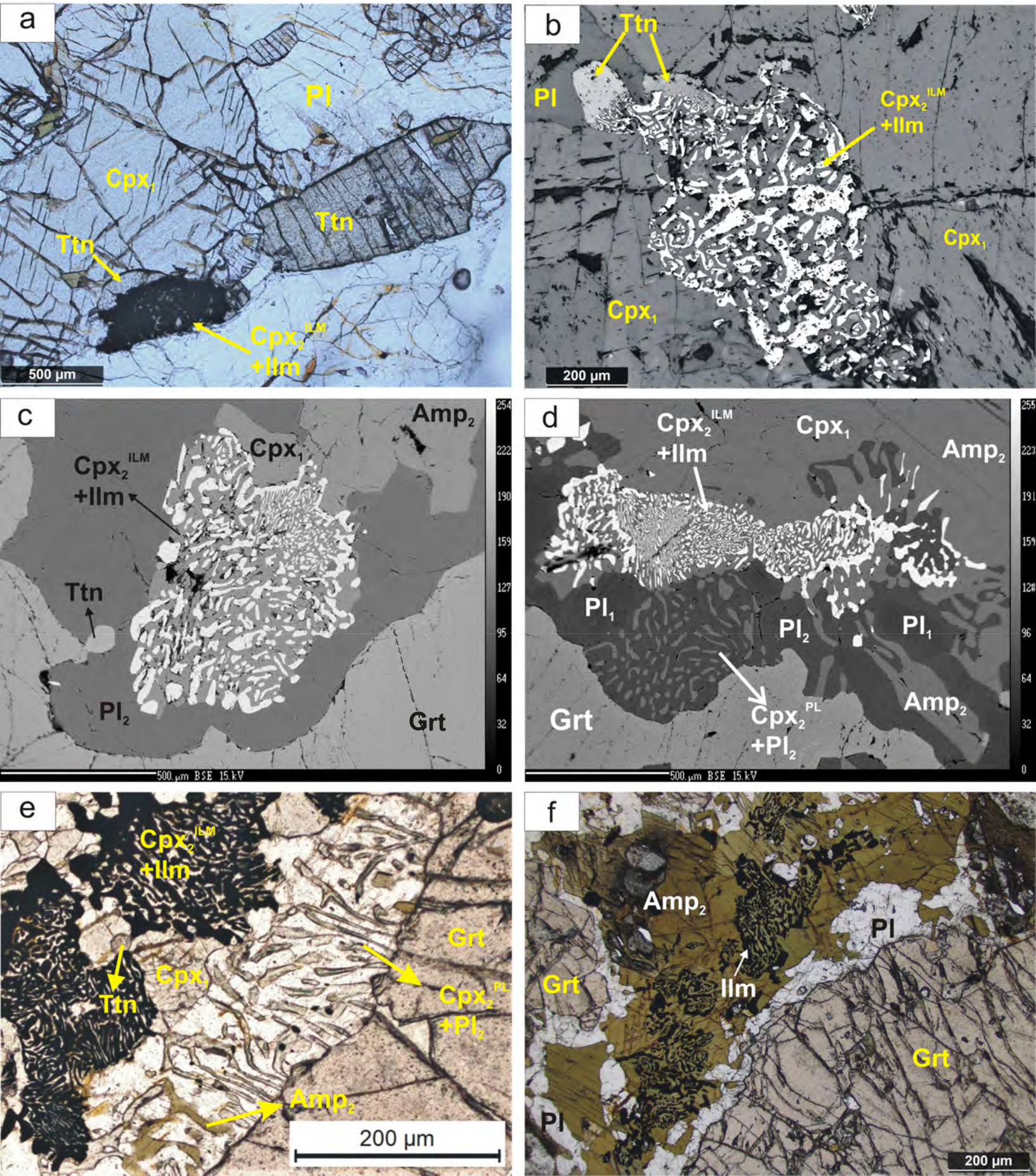
a
Pl
Cpx1
Ttn
Ttn
Cpx2 ILM +Ilm
500 µm
b
Ttn
Pl
Cpx2 ILM +Ilm
Cpx1
Cpx1
200 µm
c
Amp2
Cpx1
Cpx2 ILM +Ilm
Ttn
Pl2
Grt
500 µm BSE 15 kV
d
Cpx2 ILM +Ilm
Cpx1
Amp2
Pl1
Pl2
Pl1
Grt
Cpx2 PL +Pl2
Amp2
500 µm BSE 15 kV
e
Cpx2 ILM +Ilm
Grt
Cpx1
Ttn
Cpx2 PL +Pl2
Amp2
200 µm
f
Amp2
Pl
Grt
Ilm
Grt
Pl
200 µm

# Figure 4

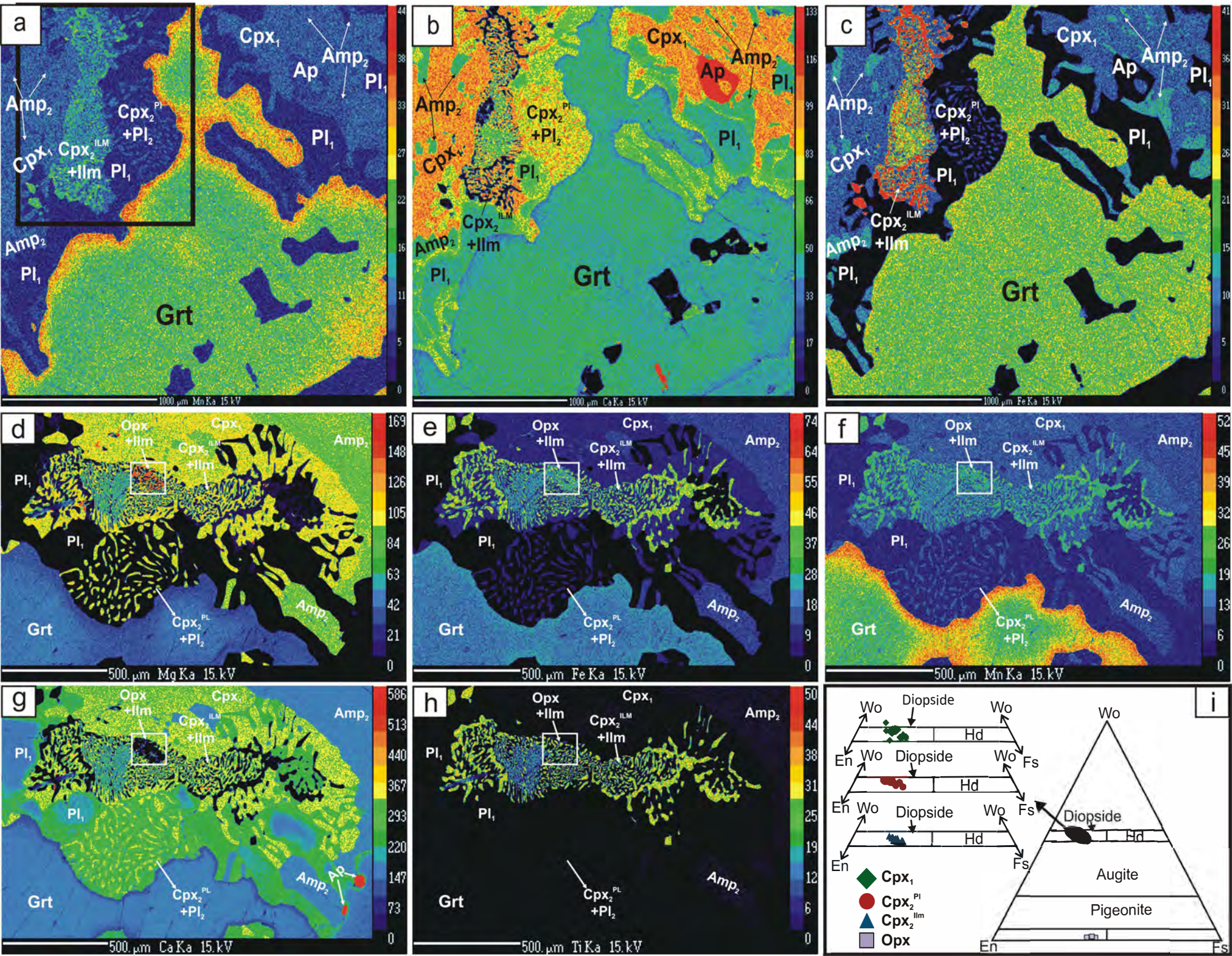
a
Cpx1
Amp2
Ap
Pl1
Cpx2 PI +Pl2
Cpx2 ILM +Ilm
Grt
1000 µm Mn Ka 15 kV
b
1000 µm Ca Ka 15 kV
c
1000 µm Fe Ka 15 kV
d
Opx +Ilm
Cpx2 PL +Pl2
500 µm Mg Ka 15 kV
e
500 µm Fe Ka 15 kV
f
500 µm Mn Ka 15 kV
g
500 µm Ca Ka 15 kV
h
500 µm Ti Ka 15 kV
i
Wo
Diopside
Hd
En
Fs
Augite
Pigeonite
Cpx1
Cpx2 PI
Cpx2 Ilm
Opx

Figure 5

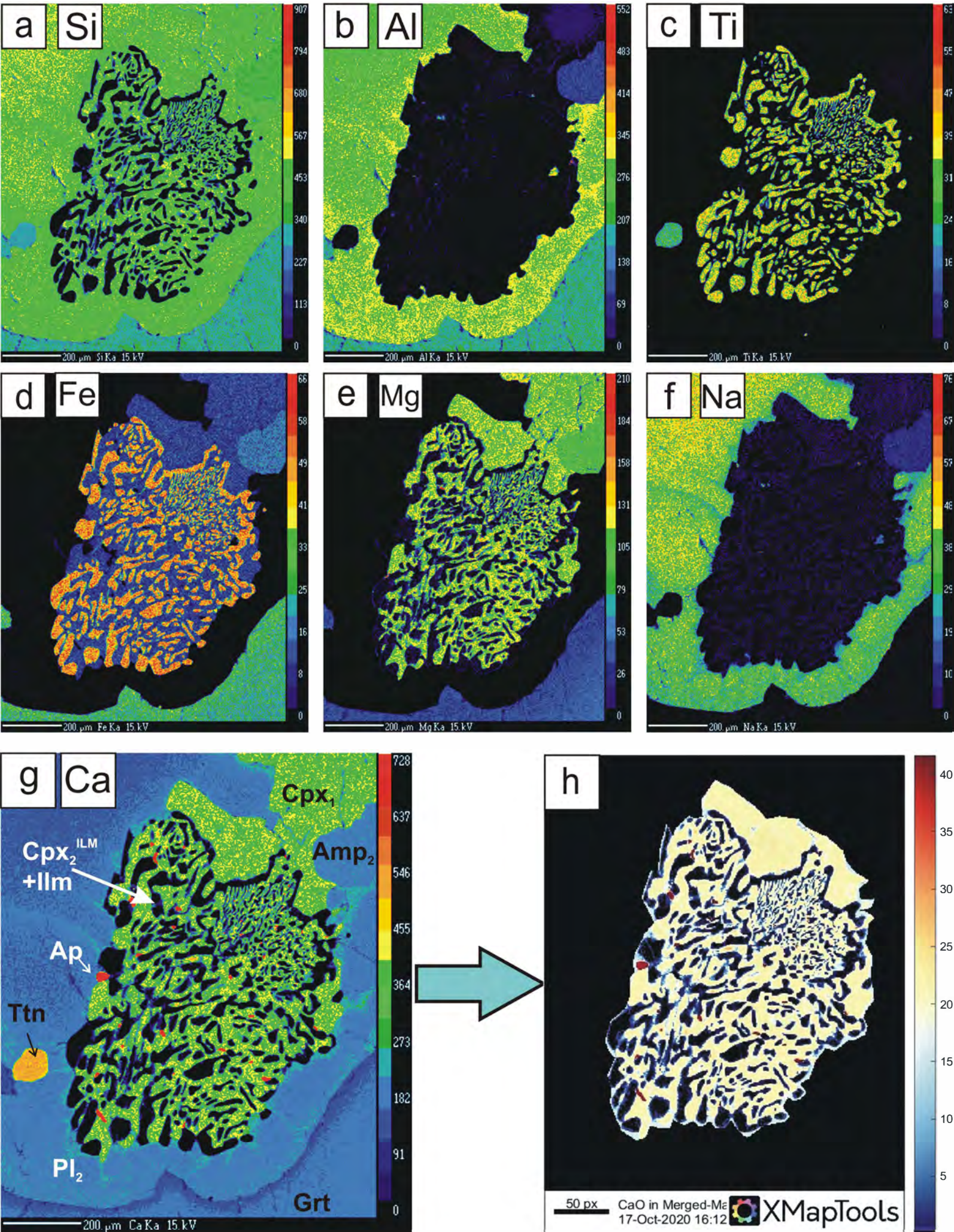
a Si
907
794
680
567
453
340
227
113
0
200 µm Si Ka 15 kV
b Al
552
483
414
345
276
207
138
69
0
200 µm Al Ka 15 kV
c Ti
200 µm Ti Ka 15 kV
d Fe
66
58
49
41
33
25
16
8
0
200 µm Fe Ka 15 kV
e Mg
210
184
158
131
105
79
53
26
0
200 µm Mg Ka 15 kV
f Na
200 µm Na Ka 15 kV
g Ca
Cpx1
Cpx2 ILM +Ilm
Amp2
Ap
Ttn
Pl2
Grt
728
637
546
455
364
273
182
91
0
200 µm Ca Ka 15 kV
h
40
35
30
25
20
15
10
5
50 px
CaO in Merged-Ma
17-Oct-2020 16:12
XMapTools

# Figure 6

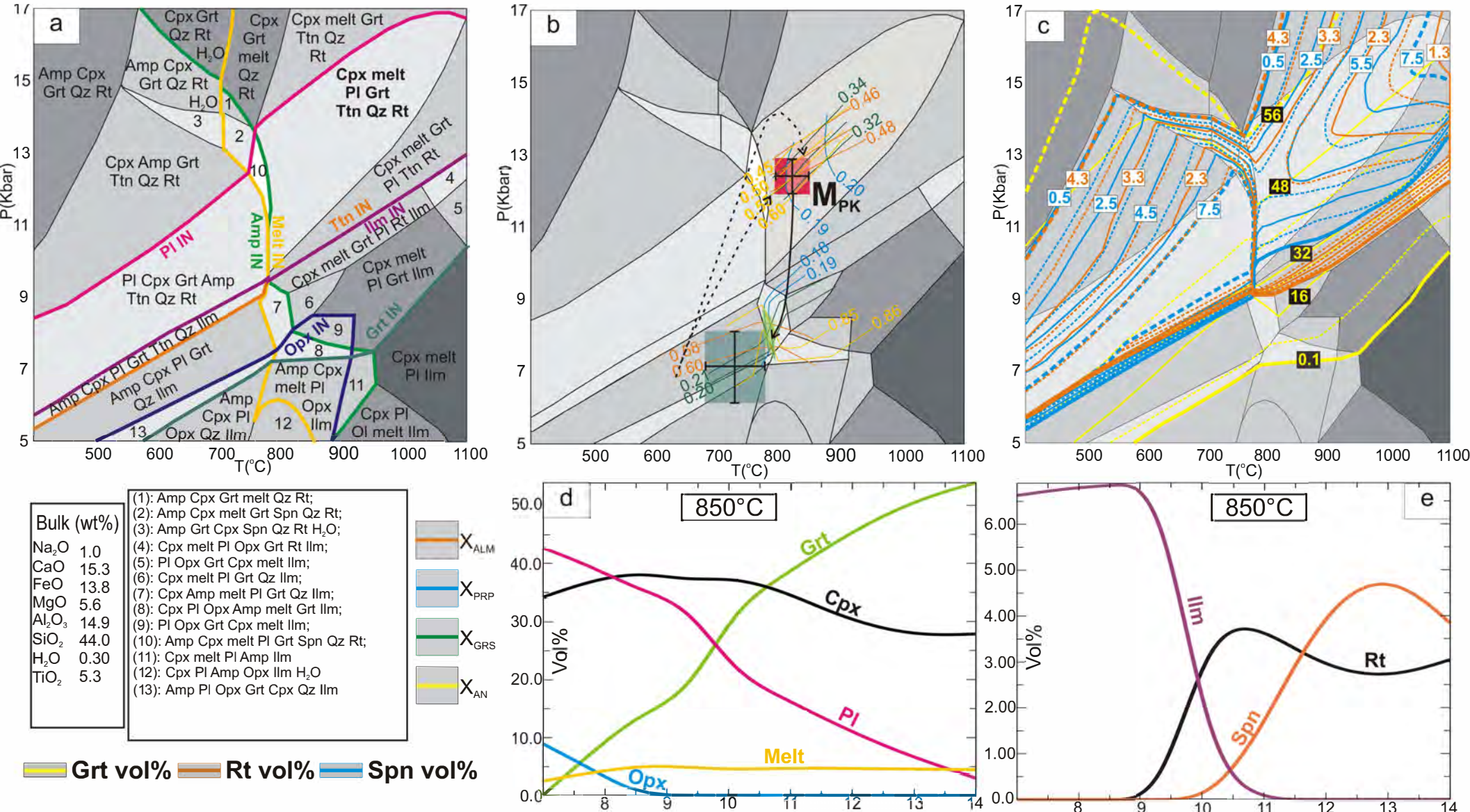
a
b
c
d
e
P(Kbar)
T(°C)
Amp Cpx Grt Qz Rt
Cpx Grt Qz Rt
Cpx Grt melt Qz Rt
Cpx melt Grt Ttn Qz Rt
Cpx melt Pl Grt Ttn Qz Rt
Cpx Amp Grt Ttn Qz Rt
Cpx melt Grt Pl Ttn Rt
Pl Cpx Grt Amp Ttn Qz Rt
Cpx melt Grt Pl Rt Ilm
Cpx melt Pl Grt Ilm
Amp Cpx Pl Grt Ttn Qz Ilm
Amp Cpx Pl Grt Qz Ilm
Amp Cpx melt Pl
Cpx melt Pl Ilm
Amp Cpx Pl Opx Qz Ilm
Opx Ilm
Cpx Pl Ol melt Ilm
Pl IN
Amp IN
Melt IN
Ttn IN
Ilm IN
Opx IN
Grt IN
M PK
850°C
Grt
Cpx
Pl
Melt
Opx
Vol%
Ilm
Rt
Spn
Bulk (wt%)
Na2O 1.0
CaO 15.3
FeO 13.8
MgO 5.6
Al2O3 14.9
SiO2 44.0
H2O 0.30
TiO2 5.3
(1): Amp Cpx Grt melt Qz Rt;
(2): Amp Cpx melt Grt Spn Qz Rt;
(3): Amp Grt Cpx Spn Qz Rt H2O;
(4): Cpx melt Pl Opx Grt Rt Ilm;
(5): Pl Opx Grt Cpx melt Ilm;
(6): Cpx melt Pl Grt Qz Ilm;
(7): Cpx Amp melt Pl Grt Qz Ilm;
(8): Cpx Pl Opx Amp melt Grt Ilm;
(9): Pl Opx Grt Cpx melt Ilm;
(10): Amp Cpx melt Pl Grt Spn Qz Rt;
(11): Cpx melt Pl Amp Ilm
(12): Cpx Pl Amp Opx Ilm H2O
(13): Amp Pl Opx Grt Cpx Qz Ilm
XALM
XPRP
XGRS
XAN
Grt vol%
Rt vol%
Spn vol%

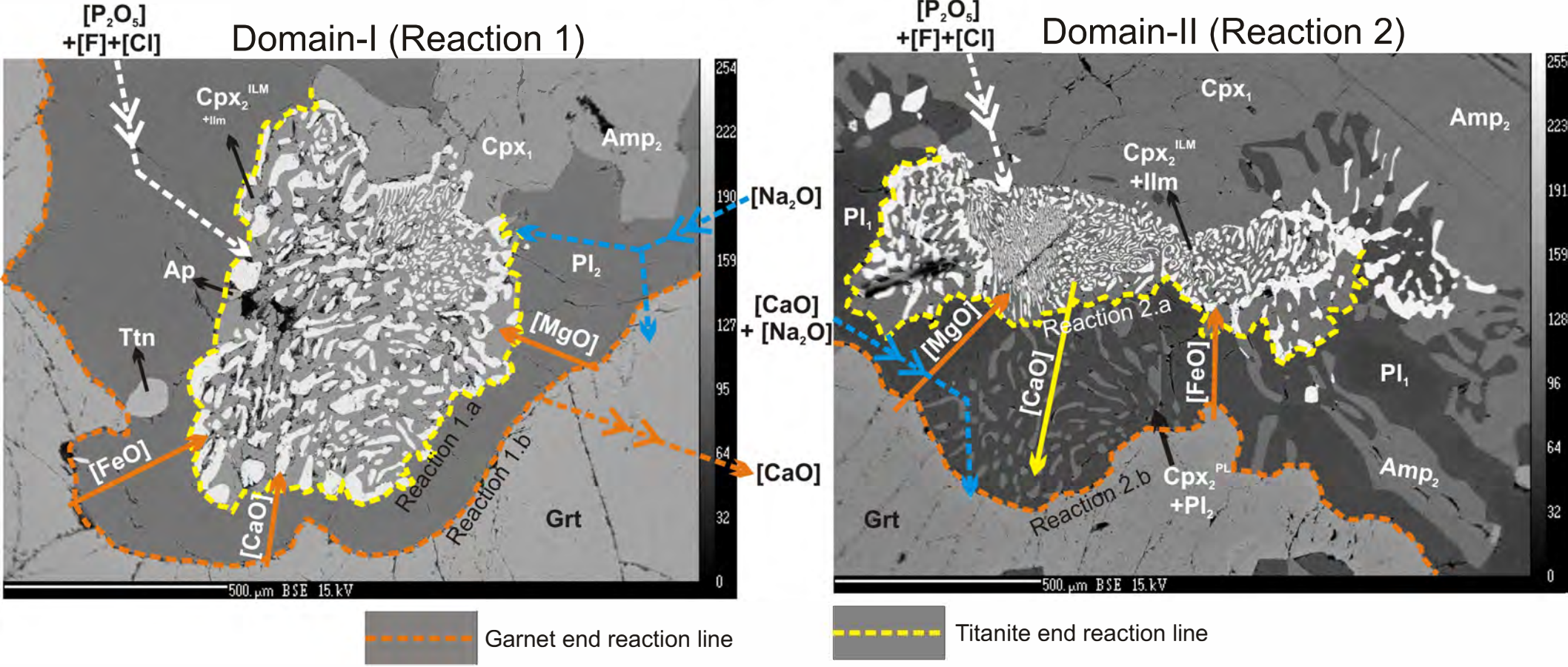
[P2O5]
+[F]+[Cl]
Domain-I (Reaction 1)
Cpx2 ILM +Ilm
Cpx1
Amp2
Ap
Ttn
Pl2
[Na2O]
[CaO]
+ [Na2O]
[MgO]
[FeO]
[CaO]
Reaction 1.a
Reaction 1.b
Grt
500 µm BSE 15 kV
254
222
190
159
127
95
64
32
0
[P2O5]
+[F]+[Cl]
Domain-II (Reaction 2)
Cpx1
Amp2
Cpx2 ILM +Ilm
Pl1
[MgO]
Reaction 2.a
[CaO]
[FeO]
Pl1
Amp2
Grt
Reaction 2.b
Cpx2 PL +Pl2
500 µm BSE 15 kV
255
223
191
159
128
96
64
32
0
Garnet end reaction line
Titanite end reaction line

Figure -7